

# Long-time equilibration can determine transient thermality

Karen V. Hovhannisyan,<sup>1,\*</sup> Somayyeh Nemati,<sup>1</sup> Carsten Henkel,<sup>1</sup> and Janet Anders<sup>1,2,†</sup>

<sup>1</sup>*University of Potsdam, Institute of Physics and Astronomy,  
Karl-Liebknecht-Str. 24-25, 14476 Potsdam, Germany*

<sup>2</sup>*Department of Physics and Astronomy, University of Exeter, Stocker Road, Exeter EX4 4QL, UK*

When two initially thermal many-body systems start interacting strongly, their transient states quickly become non-Gibbsian, even if the systems eventually equilibrate. To see beyond this apparent lack of structure during the transient regime, we use a refined notion of thermality, which we call g-local. A system is g-locally thermal if the states of all its small subsystems are marginals of global thermal states. We numerically demonstrate for two harmonic lattices that whenever the total system equilibrates in the long run, each lattice remains g-locally thermal at all times, including the transient regime. This is true even when the lattices have long-range interactions within them. In all cases, we find that the equilibrium is described by the generalized Gibbs ensemble, with three-dimensional lattices requiring special treatment due to their extended set of conserved charges. We compare our findings with the well-known two-temperature model. While its standard form is not valid beyond weak coupling, we show that at strong coupling it can be partially salvaged by adopting the concept of a g-local temperature.

## I. INTRODUCTION

Equilibration and thermalization in closed quantum many-body systems have received a lot of attention during the past two decades, leading to tremendous successes in understanding the conditions under which equilibration happens [1–4] and the properties of the (sometimes thermal) equilibrium itself [1, 3, 5–8]. However, only two general “expected behaviors” are known about the *transient* regime [9]. First, for a small subsystem weakly coupled to the rest of the large system one expects Markovianity of the dynamics [10, 11] [12]. Second, when two well-separated relaxation timescales are present, some observables will typically show pre-thermalization [4, 13–16]. In this work, we propose a qualitatively new transient behavior for a generic physical setting and then provide numerical evidence demonstrating that it indeed occurs in harmonic lattices.

The setting we consider—generic in mesoscopic and macroscopic physics—is that of two large quantum many-body systems,  $X = A$  and  $B$ , of comparable size. Initially they do not interact and start uncorrelated, each in a *global* Gibbs state

$$\tau(T_X, H_X) := \frac{1}{Z_X} e^{-H_X/T_X}. \quad (1)$$

Here  $H_X$  is the Hamiltonian of  $X$  and  $T_X$  is a temperature in units  $k_B = 1$ , with  $Z_X := \text{Tr}[e^{-H_X/T_X}]$  being the partition function. Because this (standard) definition focuses on each whole many-body system, we call it *global thermality*.

Then, in a sudden quench, coupling between the two systems is switched on, as depicted in Fig. 1. The total system state  $\rho_{AB}(t)$  then evolves under the unitary

evolution generated by the post-quench constant total Hamiltonian  $H_{\text{tot}} := H_A \otimes \mathbb{I}_B + \mathbb{I}_A \otimes H_B + H_{\text{int}}$ , where  $H_{\text{int}}$  is the interaction term and  $\mathbb{I}_X$  is the identity operator on the Hilbert space of  $X$ .

The textbook expectation for weakly coupled macroscopic systems  $A$  and  $B$  is that the evolution progresses quasistatically and thus each of them retains global thermality [see Eq. (1)] at all times  $t$ , while gradual heat exchange brings the systems to a shared thermal equilibrium [17]. In other words, the individual states of  $A$  and  $B$  obey  $\rho_X(t) \approx \tau(T_X(t), H_X)$ , with evolving temperatures  $T_X(t)$  such that  $T_A(t), T_B(t) \rightarrow T^{\text{eq}}$ . When the coupling is such that thermal gradients arise within  $X$ , still, the expectation would be that each small, localized portion of  $X$  maintains a Gibbs state with respect to its local Hamiltonian [17–20] at all times. Down to the mesoscopic scale, the assumption of instantaneous (local) thermality is the cornerstone of the two-temperature model (TTM) in solid-state physics [21–24]. It is designed to describe the joint dynamics of electrons and phonons in a solid after the electrons are suddenly heated up by radiation. Due to its simplicity, the TTM has been extensively employed for fitting the results of experiments and *ab initio* calculations [23–30].

However, when the coupling between and within the two global systems is not weak, then neither the assumption of global thermality, nor that of local thermality, of each  $A$  and  $B$  is valid any longer [31–34]. Taking this general observation as a starting point, in this article we ask whether, and in what sense, these many-body systems may nevertheless keep appearing globally thermal when observed locally, i.e., on small subsystems.

To answer this, we begin by stating a new framework of thinking about thermality in Section II, which subsumes the standard definition of thermality (1). It relies on both global and local properties of the system, and hence defines a new concept of thermality which we call “g-local.” Its efficacy is demonstrated on harmonic lattices, a realistic yet efficiently simulable system [10, 11, 17, 35, 36],

\* karen.hovhannisyan@uni-potsdam.de

† janet@qipc.org

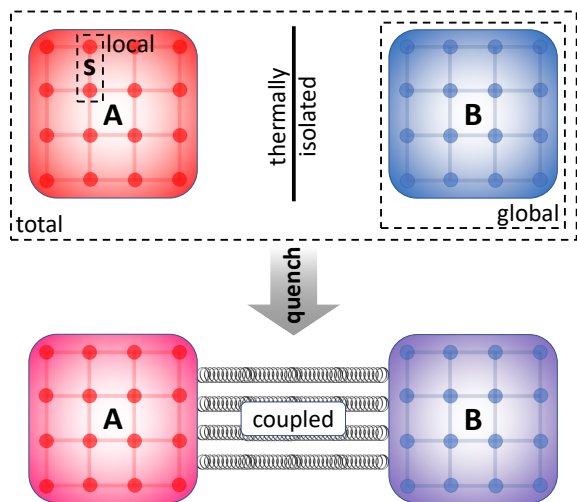


FIG. 1: (**General setup.**) Two quantum many-body systems,  $X = A$  and  $B$ , start non-interacting and uncorrelated, each in a (global) Gibbs state Eq. (1). Then, in a sudden quench, interaction between them is switched on. As a result, neither  $A$  nor  $B$  will generally maintain global thermality during the joint post-quench unitary evolution. Here we establish in what sense a more local notion of thermality may be maintained during the evolution. Dashed boxes illustrate our scale terminology: “total” refers to  $AB$ -wide, “global” to either  $A$  or  $B$ , and “local” pertains to small subsystems  $s$  within  $A$  or  $B$ .

which we introduce in Section III. By numerically solving their dynamics, we establish in Section IV how well g-local thermality captures the instantaneous states of the co-evolving systems. In Section V, we look at the process of equilibration and discuss the subtleties of constructing the generalized Gibbs ensemble (GGE) describing it. We close with a brief discussion of implications for the validity of the TTM ansatz in Section VI, before concluding in Section VII.

Our main result is that *if* local observables of the total system  $AB$  equilibrate for long times, then each  $A$  and  $B$  maintain g-local thermality to a very good approximation at all times, including the transient regime. Moreover, this behavior is valid at all coupling strengths, including very strong coupling. This all-time validity of g-local thermality is surprising because, in general, the dynamics during the transient regime is thought to be structureless. The result thus fleshes out a novel “expected behavior” for the process of joint equilibration of two large systems.

## II. G-LOCAL THERMALITY

Consider a state  $\rho_X$  of a many-body system  $X$  and a small local subsystem  $s \subset X$ ; see Fig. 1. We ask whether a temperature  $T$  exists such that the reduced state  $\rho_s =$

$\text{Tr}_{X \setminus s}[\rho_X]$  of  $s$  obeys

$$\rho_s \stackrel{?}{=} \text{Tr}_{X \setminus s}[\tau(T, H_X)], \quad (2)$$

where the partial trace is taken over all of  $X$  except  $s$ . If this condition is obeyed, then we say that  $X$  is “g-locally thermal at  $s$ .” The term “g-local” is to emphasize that, while  $\rho_s$  is a *local* quantity, it contains information about the *global*  $\tau(T, H_X)$  due to non-negligible interactions within  $X$ . Furthermore if  $X$  is g-locally thermal at each small subsystem, then we call  $X$  “g-locally thermal.” If in addition  $T$  is the same for all of them, then we call  $X$  “uniformly g-locally thermal.” Otherwise, when  $T$  varies depending on the subsystem, we say that  $X$  is “g-locally thermal with a gradient.”

Note that condition (2) is not to be confused with subsystem  $s$  being in a Gibbs state  $\tau(T, H_s)$  at  $T$  with respect to its local (bare) Hamiltonian  $H_s$ . Indeed, it is well-known that  $\rho_s$  can differ significantly from  $\tau(T, H_s)$  [8, 31–33, 37–42]. Instead, partially reduced states of global Gibbs states

$$\tau_s^{\text{MF}}(T) := \text{Tr}_{X \setminus s}[\tau(T, H_X)] \quad (3)$$

are known as “mean force (Gibbs) states” [7, 43–45]. With this definition, the condition of “g-local thermality of  $X$ ” can be compactly expressed as

$$\rho_s \stackrel{!}{=} \tau_s^{\text{MF}}(T), \quad \forall s \subset X, \quad (4)$$

where the  $s$  are small subsystems.

However, in most realistic scenarios one cannot expect the equality (4) to be exact. Thus, it is sensible to introduce an effective g-local temperature  $T_s^{\text{eff}}$  for each subsystem  $s \subset X$  as that of the mean force state  $\tau_s^{\text{MF}}(T)$  that is closest to  $\rho_s$ . Namely,

$$T_s^{\text{eff}} := \arg \min_T \mathcal{D}[\rho_s, \tau_s^{\text{MF}}(T)], \quad (5)$$

where as a measure of distance  $\mathcal{D}$  between the two states, we chose the Bures metric [46] (see Appendix A for the definition). The distance

$$\mathcal{D}_s^{\min} := \min_T \mathcal{D}[\rho_s, \tau_s^{\text{MF}}(T)] \quad (6)$$

then measures to what extent  $\rho_s$  deviates from the optimal mean-force Gibbs state. In what follows, we will use the dual quantity, the *fidelity* [46],

$$\mathcal{F}_s^{\max} := [1 - (\mathcal{D}_s^{\min})^2/2]^2 \leq 1, \quad (7)$$

and call this the degree of g-local thermality of  $X$  at  $s$ . The fidelity is 1 *iff* the two states  $\rho_s$  and  $\tau_s^{\text{MF}}$  are equal, in which case  $T_s^{\text{eff}}$  turns into a proper g-local temperature for  $s$ . Therefore, the higher the  $\mathcal{F}_s$ , the closer the local system  $s$  is to having a well-defined g-local temperature; see Eq. (5).

The pair  $(T_s^{\text{eff}}, \mathcal{F}_s^{\max})$  thus fully characterizes the g-local thermality of  $X$  at subsystem  $s$ . If the  $T_s^{\text{eff}}$  for

essentially all small  $s \subset X$  are approximately equal to each other, and all  $\mathcal{F}_s^{\max}$ 's are close to 1 (within a chosen error [47]), then  $\rho_X$  (or  $X$  itself) is g-locally thermal, with uniform temperature  $T_X^{\text{eff}}$ . In section IV, we will use  $T_s^{\text{eff}}$  and  $\mathcal{F}_s^{\max}$  to assess the g-local thermality of each of the two global systems,  $A$  and  $B$ , of comparable size  $N$ , during their joint evolution.

Unmistakably, our framework is inspired by the equivalence of ensembles [48–52] and canonical typicality [3, 53, 54]. The difference is in how temperature is defined. There, the effective temperature  $T_X^{\text{eff,can}}$  is determined by equating the mean energies, i.e.,

$$\text{Tr}[\tau(T_X^{\text{eff,can}}, H_X)H_X] = \text{Tr}[\rho_X H_X], \quad (8)$$

and it is shown that Eq. (2) is satisfied for  $T = T_X^{\text{eff,can}}$  under certain conditions on  $H_X$  and  $\rho_X$ . This approach is thus energy-centric and global:  $T_X^{\text{eff,can}}$  is the same for all subsystems. In contrast, our framework is state-centric and local: it directly accesses the marginal state of a subsystem  $s$  and defines  $T_s^{\text{eff}}$  as the solution of the optimization problem (6). The ability to define a local degree of thermality and an associated temperature at each subsystem allows our framework to accommodate systems with a temperature gradient (see Appendix D for an example), which is beyond the reach of the typicality-based approaches. Note that, when  $H_X$  is a sum of local terms and the system is g-locally thermal with a uniform g-local temperature  $T_X^{\text{eff}}$ , then the two temperatures coincide:  $T_X^{\text{eff,can}} = T_X^{\text{eff}}$  (see Appendix B).

Lastly, when the size of the system  $X$  is finite, then Eq. (2) will hold for a system in a canonically typical state only approximately, with the correction going to zero as  $N_s/N_X \rightarrow 0$ , where  $N_s$  and  $N_X$  are the numbers of sites in  $s$  and  $X$ , respectively. Similarly, in our framework, we expect  $\mathcal{D}_s^{\min}$  to also have a positive contribution stemming from the small parameter  $N_s/N_X$  in realistic scenarios. This finite-size contribution will likely be a highly complex function of  $N_s/N_X$  [54, 55], and the line between “small” and “big” subsystems will be drawn by this system- and situation-dependent contribution and one’s error tolerance. Importantly, the finite-size effect will in general not be the only factor contributing to  $\mathcal{D}_s^{\min}$ .

### III. SETUP AND MODEL

As mentioned in the introduction, our setup consists of two large many-body systems,  $A$  and  $B$ , co-evolving after an interaction between them is switched on. To be able to solve the dynamics of the total system  $AB$  and demonstrate the occurrence (or absence) of g-local thermality of each,  $A$  and  $B$ , we chose harmonic lattices. Despite their simplicity, these systems are routinely used to approximate various physical systems [10, 11, 17, 35, 36]. At the same time, the dynamics of the Gaussian states in

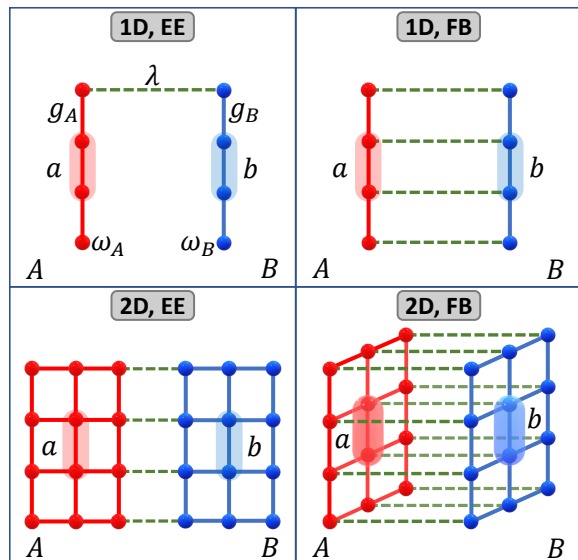


FIG. 2: (**Model schematic.**) Systems  $A$  (red) and  $B$  (blue) are here modeled as 1D (**top row**) or 2D (**bottom row**) harmonic lattices. Each site (circles) denotes a local oscillator of frequency  $\omega_X$  which is coupled to its neighbors with strength  $g_X$  (solid lines), cf. Eq. (9). While only nearest-neighbor interactions are depicted, our results apply also to long-range interacting systems. Inter-system coupling (dashed green lines) with strength  $\lambda$  occurs either only at the system edges—as shown in the **left column** (edge-edge (EE) coupling), or at all sites—as shown on the **right column** (full-body (FB) coupling), see Eq. (11). In all panels, example subsystems  $a$  and  $b$  are depicted, at which g-local thermality of each,  $A$  and  $B$ , will be assessed in Sec. IV.

these systems admit a numerically efficient phase-space representation [56–58], allowing us to directly simulate few-hundred-particle lattices.

Each global system is a 1D or 2D translation-invariant open-ended lattice, see Fig. 2, with Hamiltonian

$$H_X = \sum_{\nu} \left[ \frac{\omega_X^2 q_{X,\nu}^2}{2} + \frac{p_{X,\nu}^2}{2} \right] + \sum_{\nu, \nu'} G_X^{\nu, \nu'} q_{X,\nu} q_{X,\nu'}, \quad (9)$$

where  $\nu$  enumerates the sites in lattice  $X$ ,  $\omega_X$  is the on-site frequency of each site, and all masses are set to 1. The intra-system coupling function,  $G_X^{\nu, \nu'}$ , depends only on the distance between the sites  $\nu$  and  $\nu'$ . Our numerical samples below explore lattices with coupling functions of the form

$$G_X^{\nu, \nu'} = \frac{g_X}{\text{dist}(\nu, \nu')^\alpha}, \quad (10)$$

where  $\text{dist}(\nu, \nu')$  is the Manhattan distance between the sites  $\nu$  and  $\nu'$ , and  $\alpha > 0$  quantifies the *range* of interactions. Nearest-neighbor interactions correspond to  $\alpha = \infty$  (and couple only sites with  $\text{dist}(\nu, \nu') = 1$ ).

We recall that  $A$  and  $B$  are large and of comparable size. Therefore, for simplicity of presentation, we choose

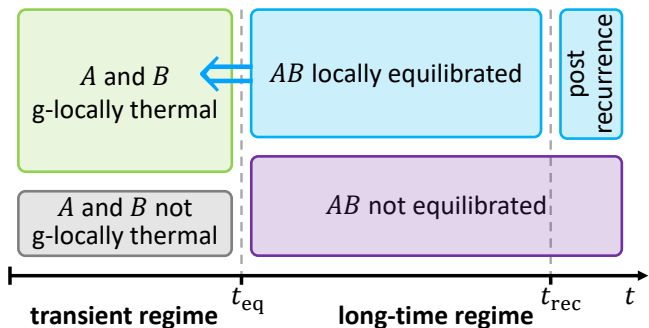


FIG. 3: (Illustration of main result.) Our main result is that **if** local equilibration occurs at long times, i.e.,  $\rho_s(t) \approx \rho_s^{\text{eq}}$  for all small subsystems  $s \subset AB$  for  $t \in [t_{\text{eq}}, t_{\text{rec}}]$  (see Sec. V), **then**  $A$  and  $B$  are g-locally thermal at any time  $t$ , also in the transient regime (see Sec. IV). Namely,  $\rho_s(t) \approx \tau_s^{\text{MF}}(T_s^{\text{eff}}(t))$ , where  $T_s^{\text{eff}}(t)$  is a time-dependent g-local temperature of subsystem  $s$  (see Sec. II). Remarkably, this result characterizes the transient regime and links it with the long-time equilibration behavior of the system.

the lattices  $A$  and  $B$  to have the same size and shape, with  $N \gg 1$  denoting the number of sites in each of them. The opposite limit, where one of the systems is much smaller than the other, say,  $N_A \ll N_B$ , is well-understood in harmonic systems.  $A$  then simply thermalizes with  $B$ , in the sense that its state tends to  $\text{Tr}_B[\tau(T_B, H_{AB})]$  (save for finite-size effects) [59, 60].

For the interaction term between  $A$  and  $B$ ,  $H_{\text{int}}$ , we consider two types of coupling: edge-edge (EE) and full-body (FB), shown in Fig. 2 for 1D and 2D lattices. For example, the FB interaction has the form

$$H_{\text{int}}^{(\text{FB})} = \lambda \sum_{\nu} q_{A,\nu} q_{B,\nu}, \quad (11)$$

where  $\lambda$  is the inter-system coupling strength, and  $\nu$  runs over *all* corresponding sites in  $A$  and  $B$ ; see the right column of Fig. 2. Given the form of Eqs. (9) and (11), the natural dimensionless coupling constants are  $g_X/\omega_X^2$  and  $\lambda/(\omega_A\omega_B)$ .

For the initial state, we take the uncorrelated state

$$\rho_{AB}(0) = \tau(T_A, H_A) \otimes \tau(T_B, H_B), \quad (12)$$

and the evolution of the joint system  $AB$  is generated by the total Hamiltonian  $H_{\text{tot}}$ . The Gaussian theory that underpins the simulation of harmonic systems has been reviewed, e.g., in Refs. [56–58]. We give a brief account of the main quantities and formulas used in our simulations in Appendix C. Using these methods, we numerically solve the dynamics of [1D,EE], [1D,FB], [2D,EE] and [2D,FB] lattices for a representative selection of the full range of parameter values for which the spectrum of  $H_{\text{tot}}$  is bounded from below [61].

Our direct simulation of the dynamics of the total system  $AB$  gives us access to  $\rho_A(t)$  and  $\rho_B(t)$ , which allows

us to analyze the g-local thermality of  $A$  and  $B$  at all times during their joint post-quench evolution.

#### IV. ALL-TIME G-LOCAL THERMALITY

We have performed a large number of numerical experiments spanning the full parameter range, and established the following: G-local thermality of  $A$  and  $B$  is guaranteed at *all times*, including transient times, whenever *all local observables of  $AB$  equilibrate dynamically at long times*; see Sec. V for further details on this requirement. This behavior occurs for all intra-lattice coupling strengths  $g_X$  and interaction ranges  $\alpha$  and inter-lattice couplings  $\lambda$ . This is the first main result of the paper. An illustration of this relation between long-time and transient behavior is shown in Fig. 3. A detailed account on how we perform the numerical proof, as well as the numerical evidence itself, can be found in Appendix E.

An immediate practical consequence of this result is that, if an experimenter monitoring a small region of the system notices that g-local thermality is violated at that location, then they can predict with certainty that the system will *not* ever equilibrate as a whole.

An example illustration of the above general result is given by Fig. 4. It shows the fidelities and effective temperatures for the case where  $A$  and  $B$  are both open-end 1D chains of 200 sites with long-range interactions within them ( $\alpha = 0.5$ ), which are coupled via a full-body (FB) interaction Hamiltonian; see Fig. 2. The plots in Fig. 4 are for subsystem  $a$  consisting of two consecutive sites in the middle of chain  $A$ , and similarly for  $b$  in  $B$ . The top panel shows the degree of g-local thermality of  $A$  at  $a$  (red), and of  $B$  at  $b$  (blue), as defined in Eq. (7). As one can see, they are close to 1 at all times, demonstrating the g-local thermality of  $A$  at  $a$  and  $B$  at  $b$ . The corresponding time-evolving effective g-local temperatures  $T_a^{\text{eff}}$  and  $T_b^{\text{eff}}$  of the small subsystems  $a$  (red) and  $b$  (blue) are shown in the bottom panel. These g-local temperatures slowly converge in time, while oscillating about each other. The apparent symmetric nature of these oscillations is due to the fact that the interaction energy remains small for the chosen set of parameters (see Sec. VI with Fig. 10 and the discussion in Appendix B).

To appreciate the nontriviality of the high values of the fidelity in Fig. 4, note that  $\lambda = 0.5\omega_A\omega_B$  corresponds to quite strong coupling. Indeed, it is close to the maximal coupling strength ( $\lambda_{\text{max}} \approx 0.695\omega_A\omega_B$ ) consistent with the requirement that  $H_{\text{tot}}$  must be bounded from below, with all the other parameters fixed. Moreover,  $\lambda/g_A = 1.875$  and  $\lambda/g_B \approx 2.222$ , which means that the coupling strongly perturbs all the nodes of both  $A$  and  $B$ . Nonetheless, both  $A$  and  $B$  maintain a high degree of g-local thermality ( $\geq 0.98$ ) at all times. For comparison, for the not-much-larger  $\lambda = 0.65\omega_A\omega_B$ ,  $\mathcal{F}_a^{\text{max}}$  and  $\mathcal{F}_b^{\text{max}}$  get as low as, respectively, 0.93 and 0.884 during the evolution.

Moreover, the all-time high degree of g-local thermality



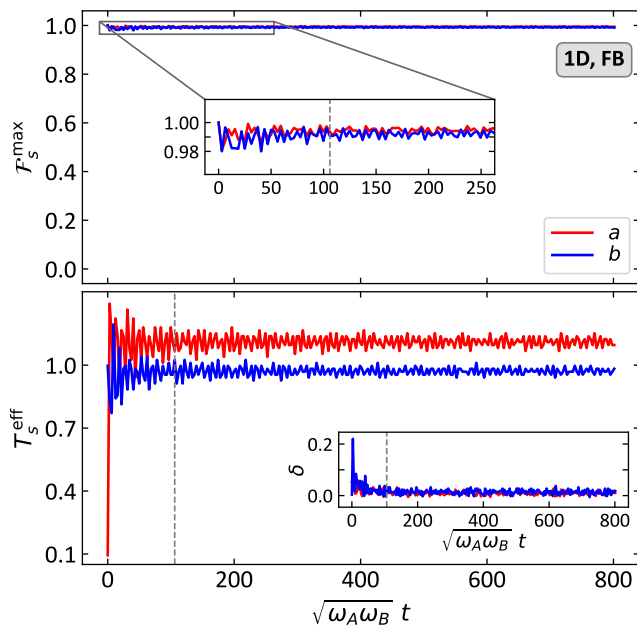


FIG. 4: (**G-local thermality of  $A$  at  $a$  and  $B$  at  $b$ .**) **Top panel:** the fidelity  $\mathcal{F}_s^{\max}$  (7), which measures the degree of g-local thermality of  $A$  at  $s = a$  (red) and of  $B$  at  $s = b$  (blue), as a function of time  $t$ . The inset zooms into the fidelity at early times. The **bottom panel** shows the corresponding effective g-local temperatures  $T_s^{\text{eff}}$  defined in Eq. (5). The inset shows the normalized difference  $\delta = (T_X^{\text{eff,can}} - T_X^{\text{eff}})/T_X^{\text{eff}}$  between the g-local and effective canonical (8) temperatures. The fidelities are close to 1, indicating that both  $A$  and  $B$  are g-locally thermal at  $a$  and  $b$ , respectively, with very good precision *at all times* during the evolution. Note that subsystems  $a$  and  $b$  settle to slightly different g-local temperatures. This plot is for  $a$  and  $b$  each consisting of two consecutive sites situated at the centers of the 1D chains  $A$  and  $B$ , respectively. The chains are  $N_A = N_B = 200$  long and interact through full-body (FB) coupling. Each chain features long-range interactions, with the decay rate  $\alpha = 1/2$  [cf. Eq. (10)]. The rest of the Hamiltonian parameters are  $\omega_A = 2$  and  $g_A/\omega_A^2 = 0.2$  for  $A$ ,  $\omega_B = 1.5$  and  $g_B/\omega_B^2 = 0.3$  for  $B$ , and the inter-chain coupling is  $\lambda/(\omega_A\omega_B) = 0.5$ . The initial temperatures are  $T_A = 0.1$  and  $T_B = 1$ . The vertical dashed lines in both panels indicate the instance at which Fig. 6 is plotted.

of  $A$  and  $B$  in Fig. 4 is in stark contrast with the quick loss of *global* thermality by them, especially at higher coupling strengths. Similarly to Eqs. (6) and (7), we quantify the degree of *global* thermality of system  $X$  as  $\mathcal{F}_X^{\max}(t) := \max_T \mathcal{F}[\rho_X(t), \tau(T, H_X)]$ . Fig. 5 shows the result for the same [1D, FB] system as in Fig. 4. One sees that the degree of global thermality in Fig. 5 quickly drops from 1 to  $\lesssim 0.05$ , which is a clear indication that the global state is not Gibbsian [62].

Lastly, we find that for most parameter choices for which the total system  $AB$  *does not* locally equilibrate

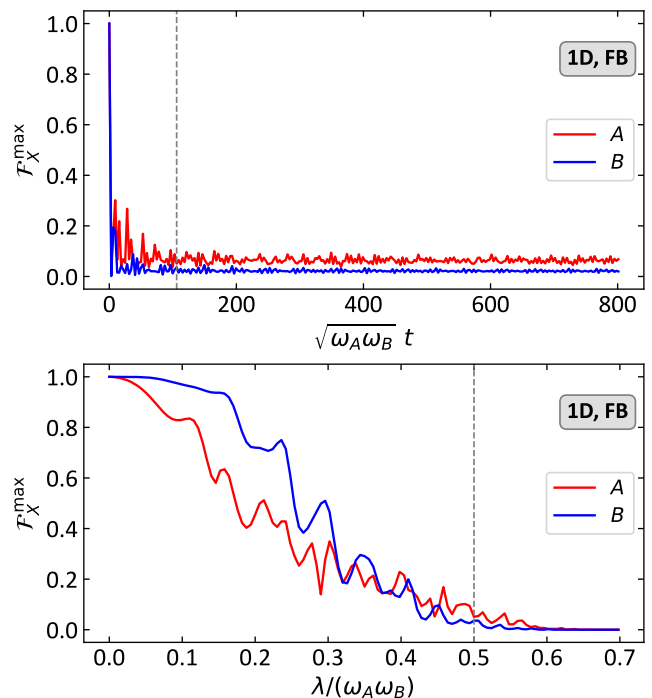


FIG. 5: (**Global non-Gibbsianity of  $A$  and  $B$ .**) **Top panel:** Fidelity  $\mathcal{F}_X^{\max}$  of the state  $\rho_X(t)$  of many-body system  $X = A, B$  with the closest global Gibbs state (1) as a function of time  $t$ . Starting from a global Gibbs state for which the fidelity is 1, the state of  $X$  deviates increasingly from Gibbs form with increasing time of interaction between  $A$  and  $B$ . The inter-chain coupling for this panel is  $\lambda/(\omega_A\omega_B) = 0.5$ , as in Fig. 4. **Bottom panel:** Fidelity  $\mathcal{F}_X^{\max}$  of the state  $\rho_X(t_0)$  at a fixed moment of time  $t_0$  as a function of the coupling strength  $\lambda$ , for  $\lambda \in [0, \lambda_{\max}]$ , where  $\lambda_{\max} \approx 0.695\omega_A\omega_B$  is the largest value allowed for  $|\lambda|$  in this configuration. The time  $\sqrt{\omega_A\omega_B} t_0 = 106$  (the vertical dashed line in the top panel) is chosen so as to allow  $AB$  to evolve considerably away from its initial state. The dashed line on this panel shows the coupling strength at which the top panel is plotted. Both panels are for the same [1D, FB] configuration, with all other parameters being the same as in Fig. 4.

at long times (purple box in Fig. 3), the global systems  $A$  and  $B$  do not develop stable g-local thermality. However, there do exist parameter values for which  $AB$  does not equilibrate, but  $A$  and  $B$  do still maintain g-local thermality at all times.

Now moving on from the specific two-site subsystems located in the respective centers of the chains, the plots in Fig. 6 show that 1D chains  $A$  and  $B$  are g-locally thermal with respect to *all* two-site subsystems  $\nu$  along the chains. Moreover, “inside the bulk”, i.e., away from the edges inwards, all two-site subsystems share the same temperature. Both  $A$  and  $B$  are thus uniformly g-locally thermal.

Of course, as the size of the subsystem  $s$  grows, the

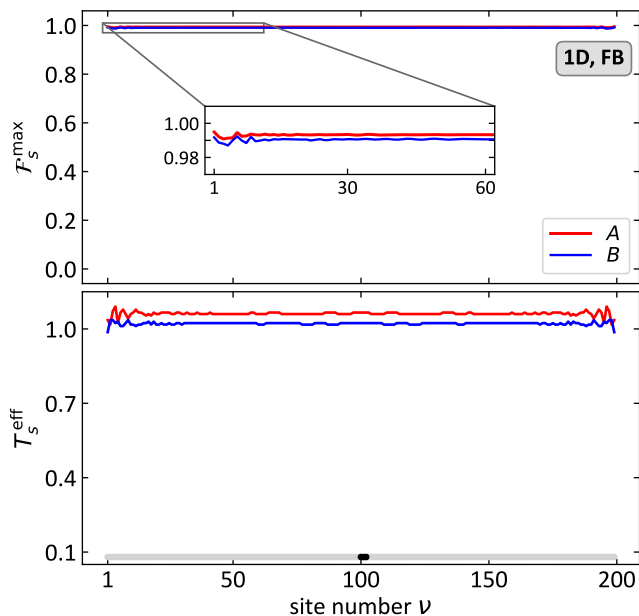


FIG. 6: (**G-local thermality with site number  $\nu$ .**) The degree of g-local thermality (**top panel**)  $\mathcal{F}_s^{\max}$  (7) of  $A$  at two-site subsystem  $s = a$  (red), and of  $B$  at  $s = b$  (blue), respectively, and (**bottom panel**) the corresponding effective temperatures  $T_s^{\text{eff}}$  (5) as a function of site number  $\nu$ . Here  $\nu = 1, \dots, N - 1$  labels *all* subsystems consisting of two neighboring sites in  $A$  and  $B$ . The fidelities are very close to 1 for all  $\nu$ . Furthermore, all subsystems  $s$  located away from the edges, i.e., those “inside the bulk”, give essentially the same g-local temperature  $T_s^{\text{eff}}$ . Together these two plots show that both  $A$  and  $B$  are uniformly g-locally thermal at *all* two-site subsystems. The “slider” (black dot) at the bottom indicates the position of subsystem  $s$  in  $X$  at which Fig. 4 is plotted. We highlight that this is just one representative snapshot of the g-local properties of  $A$  and  $B$  at any particular moment in time; here  $\sqrt{\omega_A \omega_B} t_0 = 106$ . We observe qualitatively the same plots for *any small subsystem size*, see Fig. 7, and at other time points (with varying temperatures), see Fig. 4. All other parameters are as in Figs. 5 and 4.

degree to which the system  $X$  is g-locally thermal at  $s$ ,  $\mathcal{F}_s^{\max}$ , must decrease, reaching very low values as  $N_s$  approaches  $N_X$  (see Fig. 5 which plots the fidelity for  $N_s = N_X$ ). The decrease of  $\mathcal{F}_s^{\max}$  with  $N_s$  is shown in Fig. 7, where the center of subsystem  $s$  is fixed at the center of  $X$ . The plot is a snapshot of the system taken at the same instance  $\sqrt{\omega_A \omega_B} t_0 \approx 106$  as in Fig. 6. The presented behavior is representative for all times. We see that  $\mathcal{F}_s^{\max} \geq 0.98$  for  $N_a \leq 4$  and  $N_b \leq 3$ . The effective g-local temperatures  $T_s^{\text{eff}}$  for all values of  $N_s$  are approximately equal. For larger values of time as well as for larger sizes of the global systems, both curves in Fig. 7 become flatter. However, they do not become entirely flat in the  $N_X \rightarrow \infty$  limit for all times. Thus, although

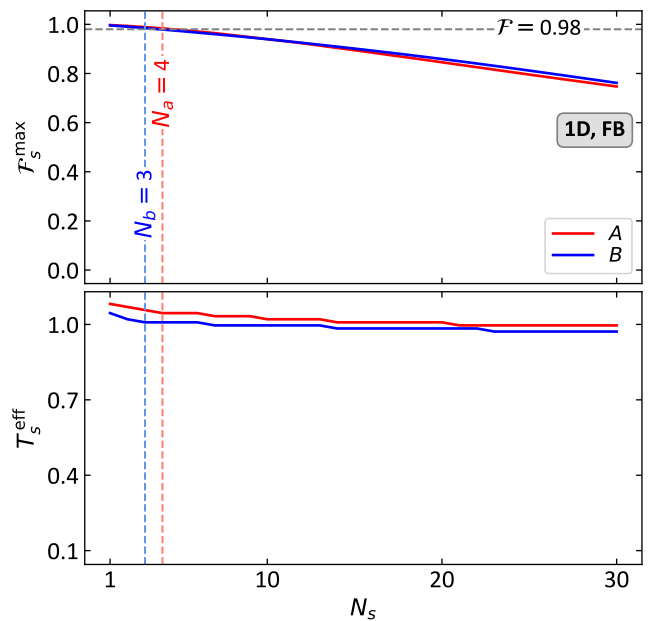


FIG. 7: (**G-local thermality with subsystem size  $N_s$ .**) **Top panel:** the degree of g-local thermality (7) of  $X$  at an  $N_s$ -site subsystem  $s$  for  $N_s = 1, 2, \dots$ . All subsystems  $s$  are centered within  $X$ , and all the other parameters are as in Figs. 5–6. The plot is taken at the instance  $\sqrt{\omega_A \omega_B} t_0 = 106$ .  $\mathcal{F}_s^{\max}$  is high ( $\geq 0.98$ ) up to subsystem sizes  $N_a = 4$  and  $N_b = 3$  for these 1D chains of  $N_A = N_B = 200$ . **Bottom panel:** the effective g-local temperatures  $T_s^{\text{eff}}$  (5) vs  $N_s$ . These values can be considered trustworthy only up to, respectively,  $N_a = 4$  and  $N_b = 3$ . Interestingly, one finds that they do not change significantly as the subsystem size goes beyond  $N_s = 4$ .

$A$  and  $B$  are indeed g-locally thermal to a good approximation at all times for  $N_X \gg 1$ , Eq. (4) does not become *exact* in the thermodynamic limit (at least not for all times).

The g-local thermality we observe is not limited to the [1D, FB] case. We find qualitatively identical behavior for the other three topological configurations [1D, EE], [2D, EE], [2D, FB] (see Fig. 1). To provide representative evidence, in Fig. 8 we show the time dependence of the fidelities and effective g-local temperatures for central 2-site subsystems  $a$  and  $b$  for the [2D, FB] case. There,  $A$  and  $B$  are 2D lattices of dimension  $26 \times 26$  (i.e.,  $N = 676$ ) with full-body interaction. These [2D, FB] plots show qualitative similarity to those for the [1D, FB] case shown in Fig. 4, with slightly better convergence compared to the 1D case. Both Figs. 4 and 8 illustrate the important possibility of the g-local temperatures of  $A$  and  $B$  not converging to the same value (cf. Sec. VI). This behavior can occur both in strong and weak coupling regimes.

For [1D, EE] and [2D, EE] configurations, we found that, while both  $A$  and  $B$  remain g-locally thermal, the systems expectedly exhibit gradients of local tempera-

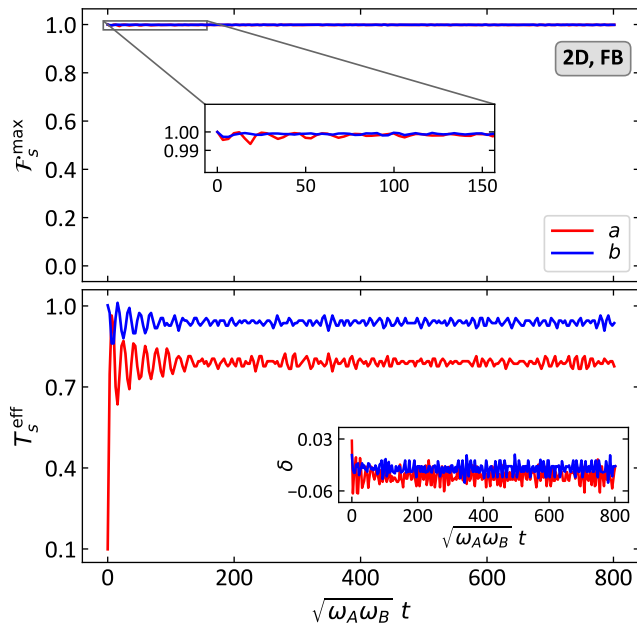


FIG. 8: (**G-local thermality for [2D, FB].**) Analog of Fig. 4 for a [2D, FB] system (bottom-right corner of Fig. 2).  $A$  and  $B$  are  $26 \times 26$  2D lattices, with nearest neighbor coupling within them [ $\alpha = \infty$  in Eq. (10)], and full-body coupling between them. The subsystems  $a$  and  $b$  are 2-site subsystems located centrally in  $A$  and  $B$ , respectively. We observe very high degrees of g-local thermality in both  $A$  and  $B$  for all times, as well as faster temperature stabilization than in Fig. 4. The inset shows the relative temperature difference  $\delta$  between  $T_X^{\text{eff}}$  and  $T_X^{\text{eff,can}}$ . Similarly to the 1D case, the subsystems  $a$  and  $b$  settle to slightly different g-local temperatures. Here the Hamiltonian parameters are  $\omega_A = 2$  and  $g_A/\omega_A^2 = 0.15$  for  $A$ ,  $\omega_B = 1.5$  and  $g_B/\omega_B^2 = 0.2$  for  $B$ , and the inter-chain coupling is  $\lambda/(\omega_A\omega_B) = 0.23$ . The initial temperatures are  $T_A = 0.1$  and  $T_B = 1$ .

tures. We discuss this in Appendix D.

**Independence from typicality.**—Finally, the novelty and unexpectedness of our all-time g-local thermality result is emphasized by that it applies to systems and situations well beyond the scope of all known results in canonical typicality and ensemble equivalence. Indeed, the most general result in that direction is the stronger ensemble equivalence proven by Brandão and Cramer [50] for lattices with short-range interactions. There it is shown that, if  $\tau(T_X^{\text{eff,can}}, H_X)$  has exponentially decaying correlations and  $\rho_X$  is not too far from  $\tau(T_X^{\text{eff,can}}, H_X)$ , then  $\rho_s$  approaches  $\tau_s^{\text{MF}}(T_X^{\text{eff,can}})$  in the thermodynamic limit for most small subsystems  $s$ . In our language, this means that  $\rho_X$  is g-locally thermal with uniform g-local temperature  $T_X^{\text{eff}} = T_X^{\text{eff,can}}$ . While the conditions under which this result applies are fairly restrictive, especially when dealing with dynamical states, it implies that our

result for FB-coupled nearest-neighbor lattices could be expected to some extent. And indeed, in the bottom inset of Fig. 8, we see that the difference between  $T_X^{\text{eff}}$  and  $T_X^{\text{eff,can}}$  remains fairly small at all times. However, long-range interacting systems, as well as situations with temperature gradient, are beyond the scope of Ref. [50] (and all other works on canonical typicality and ensemble equivalence known to us). Sure enough, we find a significant discrepancy between  $T_X^{\text{eff}}$  and  $T_X^{\text{eff,can}}$  in Figs. 4 and 11, signalling that the results of Ref. [50] do not hold. The persistent g-local thermality we observe, on the other hand, applies to all these systems and situations, which strongly suggests that it is a phenomenon fundamentally different from ensemble equivalence. We provide further context and a more detailed discussion in Appendix F.

## V. EQUILIBRATION AND THE GENERALIZED GIBBS ENSEMBLE

Recall that all-time g-local thermality of  $A$  and  $B$  is guaranteed whenever *all local states* of  $AB$  equilibrate at long times. Here we first discuss the details of this requirement and then describe how the equilibrium state relates to the generalized Gibbs ensemble (GGE).

The definition of “local equilibration” [3, 63] of the total system  $AB$  is that the reduced state  $\rho_s(t) = \text{Tr}_{AB \setminus s}[\rho_{AB}(t)]$  of each small subsystem  $s$  of  $AB$  reaches an  $\epsilon$ -neighbourhood of some  $\rho_s^{\text{eq}}$  within some finite time  $t_{\text{eq}}(\epsilon)$ , and thereafter stays in it. Typically,  $t_{\text{eq}}(\epsilon)$  will depend only weakly on the size of  $AB$ , as long as  $AB$  is large enough. Note though that, in general, the larger the relative size  $N_s/N_{AB}$  of  $s$ , the larger  $\epsilon$  one has to tolerate; see also the related discussion at the end of Sec. II.

On the other hand, for a finite system of size  $N_{AB}$ , there is always an upper time limit, the recurrence time  $t_{\text{rec}}$ , at which the local equilibration behavior is disrupted and information starts flowing back from  $AB \setminus s$  into the subsystem  $s$ . This timescale is typically a monotonically increasing function of  $N_{AB}$ . Hence, “local equilibration” of  $AB$  refers to being in equilibrium in the full time-interval  $[t_{\text{eq}}, t_{\text{rec}}]$  [64]. Numerically, we confirm local equilibration by directly calculating  $\rho_s(t)$  from  $t = 0$  to some large  $t_{\text{max}}$  and plotting the distance  $\mathcal{D}[\rho_s(t), \rho_s^{\text{GGE}}]$  against  $t$ . When this distance goes below some small  $\epsilon$  and stays there for a substantial portion of the time, then we conclude that  $\rho_s^{\text{eq}} = \rho_s^{\text{GGE}}$  (for a more precise characterization, see Appendix E 2). This procedure is done for all small  $s$ .

Representative results are shown in Fig. 9 for [1D, FB] and [2D, FB] configurations. We emphasize again that, when such local equilibration of  $AB$  occurs at long times,  $t > t_{\text{eq}}$ , then g-local thermality of  $A$  and  $B$  holds *at all times*, including the transient time interval  $[0, t_{\text{eq}}]$ .

Let us now comment on the nature of the equilibrium state itself. For an integrable system (the total system  $AB$  in our case), whenever local equilibration takes place,

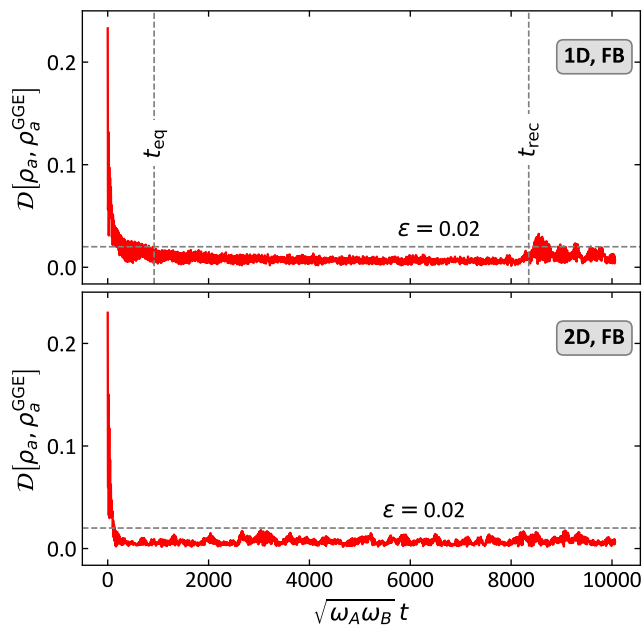


FIG. 9: **(Equilibration and timescales.) Top panel:** Equilibration of a two-site subsystem  $a$  in the center of  $A$  for [1D, FB] configuration with  $\alpha = 1.75$  and all the other parameters as in Fig. 8. Here the normal-frequency spectrum is nondegenerate and therefore the equilibrium state  $\rho_a^{\text{eq}}$  equals  $\rho_a^{\text{GGE}}$ , with the latter defined in Eq. (14). Due to the finite size of  $AB$ , equilibration never occurs exactly—one usually fixes a small  $\epsilon > 0$  and considers the system equilibrated once  $\mathcal{D}[\rho_a(t), \rho^{\text{eq}}] \leq \epsilon$ . We choose  $\epsilon = 0.02$  for this panel, and find that  $s$  is in equilibrium for  $t \in [t_{\text{eq}}, t_{\text{rec}}]$ . For times larger than the “recurrence time”  $t_{\text{rec}}$ ,  $AB$  deviates from local equilibrium. This  $t_{\text{rec}}$  grows with the size of  $AB$ . **Bottom panel:** Equilibration of a two-site subsystem at the center of  $A$  for [2D, FB] configuration with  $\alpha = 1$  and all the other parameters as in Fig. 8. The equilibrium is still described by the GGE, but one that is complemented with the additional conserved charges present in this configuration due to degeneracies in the normal-mode spectrum.

it is generically described by the so-called generalized Gibbs ensemble (GGE) [2, 3, 6, 14, 16, 65–72]. For systems with quadratic Hamiltonians (bosonic and fermionic alike), the GGE is determined only by quadratic conserved charges [68, 73, 74]. Whenever all the normal frequencies of the system are different from each other, the Hamiltonians of the normal modes, which are conserved, constitute a basis in the algebra of conserved charges. Thus, when all  $N_{AB}$  normal frequencies  $\Omega_k$  of the interacting harmonic lattice  $AB$  are distinct, the GGE takes the form

$$\rho_{AB}^{\text{GGE}} := \frac{e^{-\sum_{\kappa} \beta_{\kappa} h_{\kappa}}}{\text{Tr}[e^{-\sum_{\kappa} \beta_{\kappa} h_{\kappa}}]}, \quad (13)$$

where  $h_{\kappa} := \frac{\Omega_{\kappa}}{2} (Q_{\kappa}^2 + P_{\kappa}^2)$  are the normal-mode Hamilto-

nians ( $Q_{\kappa}$  and  $P_{\kappa}$  being the normal-mode coordinates) of  $AB$ . By definition, the total post-quench Hamiltonian can be written as  $H_{\text{tot}} = \sum_{\kappa=1}^{N_{AB}} h_{\kappa}$  (see Appendix C).

The state (13) describes the equilibrium in the sense that [64, 68]

$$t_{\text{eq}} \leq t \leq t_{\text{rec}} : \rho_s(t) \approx \text{Tr}_{AB \setminus s} [\rho_{AB}^{\text{GGE}}] := \rho_s^{\text{GGE}}, \quad (14)$$

where the approximate equality sign indicates that there will generally be a finite-size correction  $\epsilon$ . In Eq. (13),  $1/\beta_{\kappa}$  are the “generalized temperatures” that stem from the fact that the  $h_{\kappa}$ ’s are conserved in the dynamics. They are determined through the initial expectation values

$$\text{Tr}[h_{\kappa} \rho_{AB}^{\text{GGE}}] = \text{Tr}[h_{\kappa} \rho_{AB}(0)], \quad \kappa = 1, \dots, N_{AB} \quad (15)$$

(see Eq. (C21) for an explicit formula). The top panel of Fig. 9 shows local convergence to this GGE for [1D, FB] configuration.

When the spectrum of normal frequencies has degeneracies, the  $h_{\kappa}$ ’s no longer span the complete algebra of conserved charges [69, 73, 74]. More specifically, each pair  $\Omega_k = \Omega_j$  ( $k \neq j$ ) adds the conserved charge  $I_{kj} = \Omega_k (Q_k Q_j + P_k P_j)$ . Together with the  $h_{\kappa}$ ’s, these now span the complete algebra of conserved charges. Therefore, in order to correctly describe the system’s local equilibrium, the GGE needs to be complemented accordingly:  $\rho_{AB}^{\text{GGE}} \propto e^{-\sum \beta_{\kappa} h_{\kappa} - \sum \tilde{\beta}_{kj} I_{kj}}$  [69, 73, 74]. Similarly to Eq. (15), the  $\tilde{\beta}_{kj}$ ’s are determined from  $\text{Tr}[I_{kj} \rho_{AB}^{\text{GGE}}] = \text{Tr}[I_{kj} \rho_{AB}(0)]$ . Due to the presence of degeneracies, the decomposition of  $H_{AB}$  into normal modes is not unique. Conveniently, one can always choose a set of normal modes ( $\tilde{Q}_{\kappa}, \tilde{P}_{\kappa}$ ) such that all  $\text{Tr}[\tilde{I}_{kj} \rho_{AB}(0)] = 0$ , which in turn leads to  $\tilde{\beta}_{kj} = 0$  [73]. With such a choice of normal modes, the GGE again takes the form (13), now depending on the  $\tilde{I}_{kj}$ ’s only indirectly, through the conditions  $\text{Tr}[\tilde{I}_{kj} \rho_{AB}(0)] = 0$ . We follow this procedure in our numerics whenever the system has a degenerate normal frequency spectrum.

In our numerical experiments, only the [2D, FB] configuration yielded degenerate normal frequency spectra. In all other configurations, the spectrum was always nondegenerate. This might be related to the fact that the [2D, FB] is the only configuration for which  $AB$  is effectively three-dimensional (cf. Fig. 2).

That the local equilibrium of harmonic systems is described by the GGE has been established in the literature for the following two scenarios: (i) Normal frequency spectrum must be nondegenerate, but the range of interactions can be arbitrary [68]; (ii) normal frequency spectrum can be degenerate, but the interactions must be of finite range or decaying exponentially [69, 73, 74]. Sure enough, our numerics confirms that the GGE describes the equilibrium for [1D, EE], [1D, FB], [2D, EE]  $\forall \alpha$  (the  $h_{\kappa}$ ’s are sufficient) and for [2D, FB] with  $\alpha = \infty$  (the  $I_{kj}$ ’s have to be accounted for).

However, the configuration [2D, FB] with  $\alpha < 2$ , where the normal-frequency spectrum is degenerate and the interactions are of long range, is not covered by any of the



known results about harmonic systems. For this case, we establish that the equilibrium is still described by the GGE that accounts for the charges  $I_{kj}$ . The bottom panel of Fig. 9 illustrates such a situation on the example of a [2D, FB] lattice with long-range interactions ( $\alpha = 1$ ).

## VI. TWO-TEMPERATURE MODEL (TTM) AND G-LOCALITY

Let us now discuss the implications of g-local thermality for the TTM in the strong-coupling regime. The two-temperature model is widely used in solid-state physics [21–26, 75, 76] to describe a setting similar to ours. Namely, it concerns the joint thermalization of two macroscopic systems that start at different temperatures. Usually one of the systems, say  $A$ , is a free electron gas while the other,  $B$ , is a crystal lattice. However, the TTM is not specific to those systems and can be formulated generally, based on two assumptions.

First, the TTM posits that each system  $A$  and  $B$  can be described by a thermal state at all times. In our notation that would mean that the reduced states must be global Gibbs states throughout,  $\rho_A(t) = \tau(T_A(t), H_A)$  and  $\rho_B(t) = \tau(T_B(t), H_B)$ , where the temperatures  $T_A(t)$  and  $T_B(t)$  vary in time. The second assumption made by the TTM (and many of its generalizations) concerns the energy exchange between  $A$  and  $B$ . It assumes that the energy exchange is governed by a rate equation, with rates given by a Fourier-like law [21–27, 76]. In Appendix G, we write this rate equation explicitly and show that its validity is equivalent to the assumption that the temperatures of the systems,  $T_A(t)$  and  $T_B(t)$ , are differentiable functions of time that converge monotonically. Thus, the second assumption can be neatly summarized as “ $T_A(t)$  and  $T_B(t)$  monotonically approach the same value  $T^{\text{eq}}$ .” The TTM’s standard regime of validity is when  $A$  and  $B$  interact relatively weakly, whereas at strong couplings it is known to break down [28].

Two key applications of the TTM are noteworthy here. First, it allows one to determine the equilibrium temperature  $T^{\text{eq}}$  [21–23, 29, 30, 77] which is fixed by energy conservation, i.e.,

$$\langle H_A \rangle_{T_A} + \langle H_B \rangle_{T_B} = \langle H_A \rangle_{T^{\text{eq}}} + \langle H_B \rangle_{T^{\text{eq}}}, \quad (16)$$

where  $\langle H_X \rangle_T := \text{Tr}[H_X \tau(T, H_X)]$  and  $T_X$  is the initial temperature of  $X$ . The lack of accounting for the energy stored in the interaction  $H_{\text{int}}$  is a manifestation of the weak coupling assumption. Second, the rate equation allows inferring the temporal changes of the temperatures and energies of the interacting systems  $A$  and  $B$  [22]. This has been used to understand the ablation of metals following ultra-short pulses [78] and to characterize the ultrafast heat transport between electrons and phonons in multi-layers [29]. Extensions to a three-temperature model which includes their interaction with spins have proven useful in the study of ultrafast demagnetization processes [79–81].

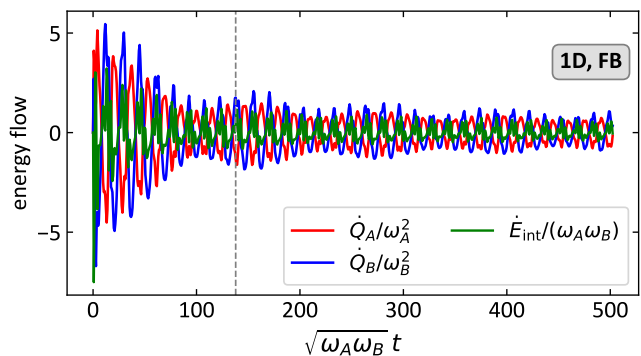


FIG. 10: (**Energy flows.**) Heat flows to each global system,  $\dot{Q}_X := d \text{Tr}[H_X \rho_X]/dt$ , and interaction energy flow,  $\dot{E}_{\text{int}}$ , as functions of time. All parameters are as in the top panel of Fig. 9. Note that the direction of heat flow from  $A \rightarrow B$  and from  $B \rightarrow A$  is oscillatory. Moreover, due to the eventual equilibration of the whole system, all energy flows slowly converge to near-zero values as time goes on beyond what is shown in the plot. This plot represents generic behavior for all four geometries in Fig 2. The vertical dashed line is chosen at  $\sqrt{\omega_A \omega_B} t_{\text{bf}} \approx 137.87$  where heat backflow occurs:  $A$  has a lower temperature than  $B$ , but loses heat ( $\dot{Q}_A < 0$ ) while  $B$  receives heat ( $\dot{Q}_B > 0$ ).

Based on our findings for harmonic lattices, we can now comment on the validity of the TTM beyond the weak coupling limit it was originally intended for. The electron–phonon setting of the original TTM corresponds to the FB coupling scenario in our setup. In Fig. 5, we see that both  $A$  and  $B$  move very quickly away from Gibbs states, even at fairly weak couplings. Hence, they have no well-defined global temperatures. This breakdown of all-time global Gibbsianity beyond the extremely weak coupling regime is not unexpected [28, 81, 82].

What is perhaps surprising is that we here find that *it is possible* to associate g-local temperatures (5) with  $A$  and  $B$  at *all times*; see Figs. 4 and 8. In this sense, the first assumption of the TTM can be rescued at strong coupling. Moreover, our finding that all-time g-local thermality also holds in the presence of temperature gradients (see Appendix D) opens the possibility of upgrading even the more general diffusive TTM [22, 26, 30, 83] to the strong coupling regime. The latter posits “local thermal equilibrium” within each lattice, i.e., that each small, localized subsystem of the lattice is in a Gibbs state with respect to its own bare Hamiltonian [19, 30]. Of course, when there is strong coupling within the lattice, the local thermality hypothesis breaks down, whereas the g-local thermality is maintained.

Regarding the second assumption of the TTM, we find that its main proposition does not hold anymore for harmonic lattices even for the extended notion of g-local temperatures. This is evidenced by Figs. 4 and 8 which clearly show that  $T_A^{\text{eff}}(t) - T_B^{\text{eff}}(t)$  is not monotonic in  $t$ .

Therefore, beyond the weak coupling limit, no TTM-type rate equation exists that would describe the time evolution of  $T_A^{\text{eff}}$  and  $T_B^{\text{eff}}$ . This is so despite the fact that heat capacities are well-defined for both  $A$  and  $B$  because they are g-locally thermal (see the discussion in Appendix B).

Nevertheless, we find that the predictive power of Eq. (16) is partially retained for harmonic lattices. Indeed, although  $T_A^{\text{eff}}$  and  $T_B^{\text{eff}}$  may in general converge to two different values (see Figs. 4 and 8), Eq. (16) remains fairly accurate with  $T^{\text{eq}}$  substituted by  $T_A^{\text{eff,eq}}$  and  $T_B^{\text{eff,eq}}$ . See a detailed discussion on this in Appendix H.

Lastly, we note that, together with the non-monotonic convergence of temperatures, the alternating direction of the heat flow shown in Fig. 10, witnesses (but does not necessitate [84]) the non-Markovian nature of the dynamics each system  $X$  is undergoing under the influence of the other. Moreover, in contrast to the predictions of the TTM, energy may sometimes flow from cold to hot, a phenomenon sometimes referred to as “backflow of heat.”

## VII. DISCUSSION

To summarize, going beyond the too restrictive demand of global thermality, we have introduced the notions of g-local thermality and the associated g-local temperatures. These characterise local subsystems while also making reference to global Gibbs states of the many-body system. We have evidenced the power of these concepts on the example of a pair of harmonic lattices with varying spatial dimensions and topologies of couplings. We found compelling numerical evidence that persistent g-local thermality of  $A$  and  $B$  at transient times is a necessary condition for  $AB$  to thermalize at long times. This is true even though  $A$  and  $B$  themselves venture far from being globally thermal, and applies to lattices  $A$  and  $B$  with both short and long range interactions within them, as well as arbitrary coupling strengths between them. This finding adds a new “expected behavior” to the short list of known results for the transient regime in the dynamics of interacting quantum many-body systems. Furthermore, for the equilibrium state itself, we found that it is described by the GGE for all configurations and interaction ranges. This includes the peculiar case of 2D lattices with full-body coupling (rendering  $AB$  three-dimensional), for which the normal-frequency spectrum is degenerate. Such systems have an extended algebra of conserved charges, and the GGE has to be constructed taking into account all those charges.

These results open several new directions. As a first step, many-body systems other than harmonic lattices may be tested numerically for the presence of g-local thermality. Further ahead, analytical arguments might be constructed that can prove the presence of transient g-local thermality given long-term equilibration for either harmonic lattices or more general many-body systems. Finally, experiments with atoms in optical lattices or trapped ions may in the future test the link between

transient g-local thermality and long-time equilibration [14–16, 65, 70, 72, 85–88].

In general, g-local thermality naturally fits into the framework of quantum thermometry [89, 90] and strong coupling thermodynamics [7, 40–42]. Performing spatially local thermometry [89–93] measures a system’s g-local temperature irrespective of whether the system state is globally thermal or g-locally thermal (see Appendix B). Such measured records give an operational meaning to g-local temperatures. Moreover, when dealing with many-body systems with local Hamiltonians, all energetic quantities are already determined by local states. Thus, those strong-coupling thermodynamics results which are derived under the assumption of global thermality [44, 94–98], will naturally extend to g-locally thermal systems. Furthermore, all-time g-local thermality may enable hydrodynamic treatment of nonequilibrium transport at strong coupling not only in the steady state [99, 100] but also in the transient. G-local thermality may also be useful in the study of local transfer in systems with non-commuting conserved charges [101, 102]. Lastly, maintained g-local thermality might lead to a type of Markovianity and local detailed balance for some observables [103] under certain conditions.

Part of the motivation for this work was to provide a microscopic justification of the two-temperature model (TTM) often used to interpret transient heat dynamics in condensed-matter systems. The TTM assumes that both systems remain globally thermal during the interaction, an assumption that generally fails when the coupling is not weak. For our model system, we saw that some of the features of the TTM can be carried over into the strong coupling regime, by updating the restrictive global thermality assumption to g-local thermality. However, at strong couplings, we saw that the g-local temperatures of  $A$  and  $B$  relax in an oscillatory fashion, and that their difference may remain nonzero. This behavior is clearly incompatible with a rate equation ansatz for heat exchange typically applied within the TTM. Nonetheless, the maintenance of g-local thermality and the ability to write a simple (approximate) energy condition for the equilibrium (g-local) temperatures akin to Eq. (16) provides a substantial generalization of the TTM to the strong coupling regime. The phenomenology we found for harmonic lattices may admittedly not be fully transposed to “hot electrons” exchanging heat with a “cold crystal lattice.” The approach we propose is however flexible enough to capture both kinds of subsystems one typically encounters in condensed-matter physics: either localized in a limited spatial domain or defined by a certain set of (coarse-grained) physical observables.

**Acknowledgments.** We thank Philipp Strasberg for interesting discussions. K.H., S.N., and J.A. are grateful for support from the University of Potsdam. J.A. gratefully acknowledges funding from the Deutsche Forschungsgemeinschaft (DFG, German Research Foundation) under Grants No. 384846402 and No. 513075417 and from the Engineering and Physical Sciences Re-

search Council (EPSRC) (Grant No. EP/R045577/1) and thanks the Royal Society for support. Open access

publication is funded by the Deutsche Forschungsgemeinschaft (DFG, German Research Foundation), Project No. 491466077.

- 
- [1] J. Gemmer, M. Michel, and G. Mahler, *Quantum Thermodynamics*, Vol. 657 (Lecture Notes in Physics, Springer, Berlin, 2004).
- [2] A. Polkovnikov, K. Sengupta, A. Silva, and M. Venugatallore, Colloquium: Nonequilibrium dynamics of closed interacting quantum systems, *Rev. Mod. Phys.* **83**, 863 (2011).
- [3] C. Gogolin and J. Eisert, Equilibration, thermalisation, and the emergence of statistical mechanics in closed quantum systems, *Rep. Prog. Phys.* **79**, 056001 (2016).
- [4] T. Mori, T. N. Ikeda, E. Kaminishi, and M. Ueda, Thermalization and prethermalization in isolated quantum systems: a theoretical overview, *J. Phys. B* **51**, 112001 (2018).
- [5] R. Orús, A practical introduction to tensor networks: Matrix product states and projected entangled pair states, *Ann. Phys.* **349**, 117 (2014).
- [6] L. Vidmar and M. Rigol, Generalized Gibbs ensemble in integrable lattice models, *J. Stat. Mech.* **2016**, 064007 (2016).
- [7] A. S. Trushechkin, M. Merkli, J. D. Cresser, and J. Anders, Open quantum system dynamics and the mean force Gibbs state, *AVS Quantum Sci.* **4**, 012301 (2022).
- [8] A. M. Alhambra, Quantum many-body systems in thermal equilibrium, (2022), [arXiv:2204.08349 \[quant-ph\]](https://arxiv.org/abs/2204.08349).
- [9] By qualifying a behavior for a setup as “expected”, we emphasize that it is proven to occur for the setup under certain restrictions, is known to sometimes occur also beyond those restrictions, but exceptions are also known. Such a state of affairs is common in statistical physics.
- [10] G. W. Ford, J. T. Lewis, and R. F. O’Connell, Quantum Langevin equation, *Phys. Rev. A* **37**, 4419 (1988).
- [11] H.-P. Breuer and F. Petruccione, *The theory of open quantum systems* (Oxford University Press, New York, 2002).
- [12] For a limited class of observables variables, a form of Markovianity can hold under more general conditions [103].
- [13] J. Berges, S. Borsányi, and C. Wetterich, Prethermalization, *Phys. Rev. Lett.* **93**, 142002 (2004).
- [14] M. Gring, M. Kuhnert, T. Langen, T. Kitagawa, B. Rauer, M. Schreitl, I. Mazets, D. Adu Smith, E. Demler, and J. Schmiedmayer, Relaxation and prethermalization in an isolated quantum system, *Science* **337**, 1318 (2012).
- [15] B. Neyenhuis, J. Zhang, P. W. Hess, J. Smith, A. C. Lee, P. Richerme, Z.-X. Gong, A. V. Gorshkov, and C. Monroe, Observation of prethermalization in long-range interacting spin chains, *Sci. Adv.* **3**, e1700672 (2017).
- [16] Y. Tang, W. Kao, K.-Y. Li, S. Seo, K. Mallayya, M. Rigol, S. Gopalakrishnan, and B. L. Lev, Thermalization near integrability in a dipolar quantum Newton’s cradle, *Phys. Rev. X* **8**, 021030 (2018).
- [17] L. D. Landau and E. M. Lifshitz, *Statistical Physics, Part I* (Pergamon, New York, 1980).
- [18] D. Polder and M. Van Hove, Theory of radiative heat transfer between closely spaced bodies, *Phys. Rev. B* **4**, 3303 (1971).
- [19] D. G. Cahill, W. K. Ford, K. E. Goodson, G. D. Mahan, A. Majumdar, H. J. Maris, R. Merlin, and S. R. Phillpot, Nanoscale thermal transport, *J. Appl. Phys.* **93**, 793 (2003).
- [20] A. I. Volokitin and B. N. J. Persson, Near-field radiative heat transfer and noncontact friction, *Rev. Mod. Phys.* **79**, 1291 (2007).
- [21] S. I. Anisimov, A. M. Bonch-Bruевич, M. A. El’yashevich, Y. A. Imas, N. A. Pavlenko, and G. S. Romanov, Effect of powerful light fluxes on metals, *Sov. Phys.-Tech. Phys.* **11**, 945 (1967).
- [22] S. I. Anisimov, B. L. Kapeliovitch, and T. L. Perel’man, Electron emission from metal surfaces exposed to ultrashort laser pulses, *Sov. Phys. JETP* **39**, 375 (1974).
- [23] D. J. Sanders and D. Walton, Effect of magnon-phonon thermal relaxation on heat transport by magnons, *Phys. Rev. B* **15**, 1489 (1977).
- [24] P. B. Allen, Theory of thermal relaxation of electrons in metals, *Phys. Rev. Lett.* **59**, 1460 (1987).
- [25] L. Jiang and H.-L. Tsai, Improved two-temperature model and its application in ultrashort laser heating of metal films, *J. Heat Transfer* **127**, 1167 (2005).
- [26] Z. Lin, L. V. Zhigilei, and V. Celli, Electron-phonon coupling and electron heat capacity of metals under conditions of strong electron-phonon nonequilibrium, *Phys. Rev. B* **77**, 075133 (2008).
- [27] W. Wang and D. G. Cahill, Limits to thermal transport in nanoscale metal bilayers due to weak electron-phonon coupling in Au and Cu, *Phys. Rev. Lett.* **109**, 175503 (2012).
- [28] L. Waldecker, R. Bertoni, R. Ernstorfer, and J. Vorberger, Electron-phonon coupling and energy flow in a simple metal beyond the two-temperature approximation, *Phys. Rev. X* **6**, 021003 (2016).
- [29] J. Pudell, A. A. Maznev, M. Herzog, M. Kronseder, C. H. Back, G. Malinowski, A. von Reppert, and M. Bargheer, Layer specific observation of slow thermal equilibration in ultrathin metallic nanostructures by femtosecond X-ray diffraction, *Nat. Commun.* **9**, 3335 (2018).
- [30] M. Herzog, A. von Reppert, J.-E. Pudell, C. Henkel, M. Kronseder, C. H. Back, A. A. Maznev, and M. Bargheer, Phonon-dominated energy transport in purely metallic heterostructures, *Adv. Funct. Mater.* **32**, 2206179 (2022).
- [31] A. Ferraro, A. García-Saez, and A. Acín, Intensive temperature and quantum correlations for refined quantum measurements, *Europhys. Lett.* **98**, 10009 (2012).
- [32] M. Kliesch, C. Gogolin, M. J. Kastoryano, A. Riera, and J. Eisert, Locality of temperature, *Phys. Rev. X* **4**, 031019 (2014).
- [33] S. Hernández-Santana, A. Riera, K. V. Hovhannisyán, M. Perarnau-Llobet, L. Tagliacozzo, and A. Acín, Lo-

- cality of temperature in spin chains, *New J. Phys.* **17**, 085007 (2015).
- [34] F. Intravaia, R. O. Behunin, C. Henkel, K. Busch, and D. A. R. Dalvit, Failure of local thermal equilibrium in quantum friction, *Phys. Rev. Lett.* **117**, 100402 (2016).
- [35] G. W. Ford, M. Kac, and P. Mazur, Statistical mechanics of assemblies of coupled oscillators, *J. Math. Phys.* **6**, 504 (1965).
- [36] N. D. Mermin and N. W. Ashcroft, *Solid State Physics* (Holt, Rinehart and Winston, New York, 1976).
- [37] L. Onsager, Theories of concentrated electrolytes, *Chem. Rev.* **13**, 73 (1933).
- [38] J. G. Kirkwood, Statistical mechanics of fluid mixtures, *J. Chem. Phys.* **3**, 300 (1935).
- [39] F. Haake and R. Reibold, Strong damping and low-temperature anomalies for the harmonic oscillator, *Phys. Rev. A* **32**, 2462 (1985).
- [40] U. Seifert, First and second law of thermodynamics at strong coupling, *Phys. Rev. Lett.* **116**, 020601 (2016).
- [41] C. Jarzynski, Stochastic and macroscopic thermodynamics of strongly coupled systems, *Phys. Rev. X* **7**, 011008 (2017).
- [42] H. J. D. Miller, Hamiltonian of mean force for strongly-coupled systems, in *Thermodynamics in the Quantum Regime: Fundamental Aspects and New Directions*, edited by F. Binder, L. A. Correa, C. Gogolin, J. Anders, and G. Adesso (Springer International Publishing, Cham, 2018) pp. 531–549.
- [43] J. D. Cresser and J. Anders, Weak and ultrastrong coupling limits of the quantum mean force Gibbs state, *Phys. Rev. Lett.* **127**, 250601 (2021).
- [44] A. Trushechkin, Quantum master equations and steady states for the ultrastrong-coupling limit and the strong-decoherence limit, *Phys. Rev. A* **106**, 042209 (2022).
- [45] C. L. Latune, Steady state in strong system-bath coupling regime: Reaction coordinate versus perturbative expansion, *Phys. Rev. E* **105**, 024126 (2022).
- [46] M. A. Nielsen and I. L. Chuang, *Quantum Computation and Quantum Information* (Cambridge University Press, Cambridge, England, 2010).
- [47] As a guideline, target values  $\mathcal{F} \geq 0.99$  for the fidelity ( $\mathcal{D} \leq 0.1$ ) are considered high in current quantum technologies (see, e.g., Refs. [104–106]).
- [48] B. Simon, *The Statistical Mechanics of Lattice Gases*, Vol. 1 (Princeton University Press, Princeton, 1993).
- [49] M. P. Müller, E. Adlam, L. Masanes, and N. Wiebe, Thermalization and canonical typicality in translation-invariant quantum lattice systems, *Commun. Math. Phys.* **340**, 499 (2015).
- [50] F. G. S. L. Brandão and M. Cramer, Equivalence of statistical mechanical ensembles for non-critical quantum systems, (2015), [arXiv:1502.03263 \[quant-ph\]](https://arxiv.org/abs/1502.03263).
- [51] H. Tasaki, On the local equivalence between the canonical and the microcanonical ensembles for quantum spin systems, *J. Stat. Phys.* **172**, 905 (2018).
- [52] T. Kuwahara and K. Saito, Gaussian concentration bound and Ensemble Equivalence in generic quantum many-body systems including long-range interactions, *Ann. Phys.* **421**, 168278 (2020).
- [53] S. Goldstein, J. L. Lebowitz, R. Tumulka, and N. Zanghì, Canonical typicality, *Phys. Rev. Lett.* **96**, 050403 (2006).
- [54] S. Popescu, A. J. Short, and A. Winter, Entanglement and the foundations of statistical mechanics, *Nat. Phys.* **2**, 754 (2006).
- [55] T. Farrelly, F. G. S. L. Brandão, and M. Cramer, Thermalization and return to equilibrium on finite quantum lattice systems, *Phys. Rev. Lett.* **118**, 140601 (2017).
- [56] G. Adesso and F. Illuminati, Entanglement in continuous-variable systems: recent advances and current perspectives, *J. Phys. A* **40**, 7821 (2007).
- [57] J. Anders, Thermal state entanglement in harmonic lattices, *Phys. Rev. A* **77**, 062102 (2008).
- [58] C. Weedbrook, S. Pirandola, R. García-Patrón, N. J. Cerf, T. C. Ralph, J. H. Shapiro, and S. Lloyd, Gaussian quantum information, *Rev. Mod. Phys.* **84**, 621 (2012).
- [59] M. Tegmark and L. Yeh, Steady states of harmonic oscillator chains and shortcomings of harmonic heat baths, *Physica A* **202**, 342 (1994).
- [60] Y. Subaşı, C. H. Fleming, J. M. Taylor, and B.-L. Hu, Equilibrium states of open quantum systems in the strong coupling regime, *Phys. Rev. E* **86**, 061132 (2012).
- [61] For fixed  $\omega_X$ 's and  $\alpha$ , the requirement that  $H_{\text{tot}}$  must be bounded from below sets an upper bound on  $|g_X|$  and  $|\lambda|$ .
- [62] Note that the stabilisation of  $\mathcal{F}_X^{\text{max}}$  does not imply that the states  $\rho_X(t)$  themselves stabilize—just their distance from the set of Gibbs states does.
- [63] N. Linden, S. Popescu, A. J. Short, and A. Winter, Quantum mechanical evolution towards thermal equilibrium, *Phys. Rev. E* **79**, 061103 (2009).
- [64] M. Cramer and J. Eisert, A quantum central limit theorem for non-equilibrium systems: exact local relaxation of correlated states, *New J. Phys.* **12**, 055020 (2010).
- [65] T. Kinoshita, T. Wenger, and D. S. Weiss, A quantum Newton's cradle, *Nature* **440**, 900 (2006).
- [66] M. Rigol, V. Dunjko, V. Yurovsky, and M. Olshanii, Relaxation in a completely integrable many-body quantum system: An ab initio study of the dynamics of the highly excited states of 1D lattice hard-core bosons, *Phys. Rev. Lett.* **98**, 050405 (2007).
- [67] M. Rigol, V. Dunjko, and M. Olshanii, Thermalization and its mechanism for generic isolated quantum systems, *Nature* **452**, 854 (2008).
- [68] T. Barthel and U. Schollwöck, Dephasing and the steady state in quantum many-particle systems, *Phys. Rev. Lett.* **100**, 100601 (2008).
- [69] M. Fagotti, On conservation laws, relaxation and pre-relaxation after a quantum quench, *J. Stat. Mech.* **2014**, P03016 (2014).
- [70] T. Langen, S. Erne, R. Geiger, B. Rauer, T. Schweigler, M. Kuhnert, W. Rohringer, I. E. Mazets, T. Gasenzer, and J. Schmiedmayer, Experimental observation of a generalized Gibbs ensemble, *Science* **348**, 207 (2015).
- [71] F. H. L. Essler and M. Fagotti, Quench dynamics and relaxation in isolated integrable quantum spin chains, *J. Stat. Mech.* **2016**, 064002 (2016).
- [72] F. Kranzl, A. Lasek, M. K. Joshi, A. Kaley, R. Blatt, C. F. Roos, and N. Yunger Halpern, Experimental observation of thermalization with noncommuting charges, *PRX Quantum* **4**, 020318 (2023).
- [73] C. Murthy and M. Srednicki, Relaxation to Gaussian and generalized Gibbs states in systems of particles with quadratic Hamiltonians, *Phys. Rev. E* **100**, 012146 (2019).
- [74] M. Gluza, J. Eisert, and T. Farrelly, Equilibration towards generalized Gibbs ensembles in non-interacting theories, *SciPost Phys.* **7**, 038 (2019).



- [75] E. Carpene, Ultrafast laser irradiation of metals: Beyond the two-temperature model, *Phys. Rev. B* **74**, 024301 (2006).
- [76] B. Liao, J. Zhou, and G. Chen, Generalized two-temperature model for coupled phonon-magnon diffusion, *Phys. Rev. Lett.* **113**, 025902 (2014).
- [77] A. von Reppert, J. Pudell, A. Koc, M. Reinhardt, W. Leitenberger, K. Dumesnil, F. Zamponi, and M. Bargheer, Persistent nonequilibrium dynamics of the thermal energies in the spin and phonon systems of an antiferromagnet, *Struct. Dyn.* **3**, 054302 (2016).
- [78] J. Byskov-Nielsen, J.-M. Savolainen, M. S. Christensen, and P. Balling, Ultra-short pulse laser ablation of copper, silver and tungsten: experimental data and two-temperature model simulations, *Appl. Phys. A* **103**, 447 (2011).
- [79] E. Beaurepaire, J.-C. Merle, A. Daunois, and J.-Y. Bigot, Ultrafast spin dynamics in ferromagnetic nickel, *Phys. Rev. Lett.* **76**, 4250 (1996).
- [80] G. Zhang, W. Hübner, E. Beaurepaire, and J.-Y. Bigot, Laser-induced ultrafast demagnetization: Femtomagnetism, a new frontier?, in *Spin Dynamics in Confined Magnetic Structures I*, edited by B. Hillebrands and K. Ounadjela (Springer, Berlin, 2002) pp. 245–289.
- [81] N. Kazantseva, U. Nowak, R. W. Chantrell, J. Hohlfeld, and A. Rebei, Slow recovery of the magnetisation after a sub-picosecond heat pulse, *Europhys. Lett.* **81**, 27004 (2007).
- [82] P. Maldonado, K. Carva, M. Flammer, and P. M. Oppeneer, Theory of out-of-equilibrium ultrafast relaxation dynamics in metals, *Phys. Rev. B* **96**, 174439 (2017).
- [83] J.-E. Pudell, M. Mattern, M. Hehn, G. Malinowski, M. Herzog, and M. Bargheer, Heat transport without heating?—An ultrafast X-Ray perspective into a metal heterostructure, *Adv. Funct. Mater.* **30**, 2004555 (2020).
- [84] R. Schmidt, S. Maniscalco, and T. Ala-Nissila, Heat flux and information backflow in cold environments, *Phys. Rev. A* **94**, 010101(R) (2016).
- [85] V. Bendkowsky, B. Butscher, J. Nipper, J. P. Shaffer, R. Löw, and T. Pfau, Observation of ultralong-range Rydberg molecules, *Nature* **458**, 1005 (2009).
- [86] J. W. Britton, B. C. Sawyer, A. C. Keith, C.-C. J. Wang, J. K. Freericks, H. Uys, M. J. Biercuk, and J. J. Bollinger, Engineered two-dimensional Ising interactions in a trapped-ion quantum simulator with hundreds of spins, *Nature* **484**, 489 (2012).
- [87] C. Gross and I. Bloch, Quantum simulations with ultracold atoms in optical lattices, *Science* **357**, 995 (2017).
- [88] H. Bernien, S. Schwartz, A. Keesling, H. Levine, A. Omran, H. Pichler, S. Choi, A. S. Zibrov, M. Endres, M. Greiner, V. Vuletic, and M. D. Lukin, Probing many-body dynamics on a 51-atom quantum simulator, *Nature* **551**, 579 (2017).
- [89] A. De Pasquale and T. M. Stace, Quantum thermometry, in *Thermodynamics in the Quantum Regime: Fundamental Aspects and New Directions*, edited by F. Binder, L. A. Correa, C. Gogolin, J. Anders, and G. Adesso (Springer International Publishing, Cham, 2018) pp. 503–527.
- [90] M. Mehboudi, A. Sanpera, and L. A. Correa, Thermometry in the quantum regime: recent theoretical progress, *J. Phys. A* **52**, 303001 (2019).
- [91] A. De Pasquale, D. Rossini, R. Fazio, and V. Giovannetti, Local quantum thermal susceptibility, *Nat. Commun.* **7**, 12782 (2016).
- [92] S. Campbell, M. Mehboudi, G. De Chiara, and M. Paternostro, Global and local thermometry schemes in coupled quantum systems, *New J. Phys.* **19**, 103003 (2017).
- [93] K. V. Hovhannisyanyan and L. A. Correa, Measuring the temperature of cold many-body quantum systems, *Phys. Rev. B* **98**, 045101 (2018).
- [94] H. J. D. Miller and J. Anders, Energy-temperature uncertainty relation in quantum thermodynamics, *Nat. Commun.* **9**, 2203 (2018).
- [95] M. Perarnau-Llobet, H. Wilming, A. Riera, R. Gallego, and J. Eisert, Strong coupling corrections in quantum thermodynamics, *Phys. Rev. Lett.* **120**, 120602 (2018).
- [96] K. V. Hovhannisyanyan, F. Barra, and A. Imparato, Charging assisted by thermalization, *Phys. Rev. Research* **2**, 033413 (2020).
- [97] C. Henkel, Heat transfer and entanglement–nonequilibrium correlation spectra of two quantum oscillators, *Ann. Phys.* **533**, 2100089 (2021).
- [98] N. Anto-Sztrikacs, F. Ivander, and D. Segal, Quantum thermal transport beyond second order with the reaction coordinate mapping, *J. Chem. Phys.* **156**, 214107 (2022).
- [99] O. A. Castro-Alvaredo, B. Doyon, and T. Yoshimura, Emergent hydrodynamics in integrable quantum systems out of equilibrium, *Phys. Rev. X* **6**, 041065 (2016).
- [100] V. B. Bulchandani, R. Vasseur, C. Karrasch, and J. E. Moore, Solvable hydrodynamics of quantum integrable systems, *Phys. Rev. Lett.* **119**, 220604 (2017).
- [101] G. Manzano, J. M. R. Parrondo, and G. T. Landi, Non-Abelian quantum transport and thermosqueezing effects, *PRX Quantum* **3**, 010304 (2022).
- [102] S. Majidy, A. Lasek, D. A. Huse, and N. Yunger Halpern, Non-Abelian symmetry can increase entanglement entropy, *Phys. Rev. B* **107**, 045102 (2023).
- [103] P. Strasberg, A. Winter, J. Gemmer, and J. Wang, Classicality, Markovianity, and local detailed balance from pure-state dynamics, *Phys. Rev. A* **108**, 012225 (2023).
- [104] C. E. Bradley, J. Randall, M. H. Abobeih, R. C. Berrevoets, M. J. Degen, M. A. Bakker, M. Markham, D. J. Twitchen, and T. H. Taminiau, A ten-qubit solid-state spin register with quantum memory up to one minute, *Phys. Rev. X* **9**, 031045 (2019).
- [105] Y. Zhou, E. M. Stoudenmire, and X. Waintal, What limits the simulation of quantum computers?, *Phys. Rev. X* **10**, 041038 (2020).
- [106] M. S. Rudolph, N. B. Toussaint, A. Katarbarwa, S. Johri, B. Peropadre, and A. Perdomo-Ortiz, Generation of high-resolution handwritten digits with an ion-trap quantum computer, *Phys. Rev. X* **12**, 031010 (2022).
- [107] H. Scutaru, Fidelity for displaced squeezed thermal states and the oscillator semigroup, *J. Phys. A* **31**, 3659 (1998).
- [108] P. Marian and T. A. Marian, Uhlmann fidelity between two-mode Gaussian states, *Phys. Rev. A* **86**, 022340 (2012).
- [109] L. Banchi, S. L. Braunstein, and S. Pirandola, Quantum fidelity for arbitrary Gaussian states, *Phys. Rev. Lett.* **115**, 260501 (2015).
- [110] R. H. Swendsen, Continuity of the entropy of macroscopic quantum systems, *Phys. Rev. E* **92**, 052110 (2015).

- [111] U. Seifert, Entropy and the second law for driven, or quenched, thermally isolated systems, *Physica A* **552**, 121822 (2020).
- [112] P. Strasberg and A. Winter, First and second law of quantum thermodynamics: A consistent derivation based on a microscopic definition of entropy, *PRX Quantum* **2**, 030202 (2021).
- [113] J. Williamson, On the algebraic problem concerning the normal forms of linear dynamical systems, *Am. J. Math.* **58**, 141 (1936).
- [114] V. I. Arnold, *Mathematical Methods of Classical Mechanics*, 2nd ed. (Springer, New York, 1989).
- [115] H. Heffner and W. H. Louisell, Transformation having applications in quantum mechanics, *J. Math. Phys.* **6**, 474 (1965).
- [116] E. G. Brown, E. Martín-Martínez, N. C. Menicucci, and R. B. Mann, Detectors for probing relativistic quantum physics beyond perturbation theory, *Phys. Rev. D* **87**, 084062 (2013).
- [117] N. Shiraishi and K. Matsumoto, Undecidability in quantum thermalization, *Nat. Commun.* **12**, 5084 (2021).
- [118] C. A. Fuchs and J. van de Graaf, Cryptographic distinguishability measures for quantum-mechanical states, *IEEE Trans. Inf. Theory* **45**, 1216 (1999).
- [119] M. Cramer and J. Eisert, Correlations, spectral gap and entanglement in harmonic quantum systems on generic lattices, *New J. Phys.* **8**, 71 (2006).
- [120] J. Barré, D. Mukamel, and S. Ruffo, Inequivalence of ensembles in a system with long-range interactions, *Phys. Rev. Lett.* **87**, 030601 (2001).
- [121] A. Campa, T. Dauxois, and S. Ruffo, Statistical mechanics and dynamics of solvable models with long-range interactions, *Phys. Rep.* **480**, 57 (2009).

## APPENDIX A: FIDELITY AND BURES DISTANCE

In definition (5), one can in principle use any metric to define the effective temperature. With any choice of metric, the resulting effective temperature will coincide with the true g-local temperature whenever the system is g-locally thermal exactly.

Since our model is Gaussian (see Appendix C), it is convenient to work with the Bures metric. It is defined as [46]

$$\mathcal{D}(\rho_1, \rho_2) := [2(1 - \sqrt{\mathcal{F}(\rho_1, \rho_2)})]^{1/2}, \quad (\text{A1})$$

where

$$\mathcal{F}(\rho_1, \rho_2) := \left( \text{Tr} \sqrt{\rho_1^{1/2} \rho_2 \rho_1^{1/2}} \right)^2 \quad (\text{A2})$$

is the quantum fidelity [46]. The reason for this preference in our case is that the fidelity can be explicitly calculated for Gaussian multimode states through their covariance matrices [107–109]; see Eqs. (C18)–(C20).

## APPENDIX B: G-LOCAL THERMALITY AND LOCAL OBSERVABLES

Let us show that, by using only local observables, one cannot differentiate between standard (globally) thermal and uniformly g-locally thermal states of many-body systems.

An observable  $O$  living in the Hilbert space of a lattice system  $X$  is called local if it can be written as

$$O = \sum_{s \subset X} O_s, \quad (\text{B1})$$

with each  $O_s$  acting nontrivially only on some spatially localized subsystem  $s$  containing at most  $k$  sites, for some fixed  $k$ . This means that one can write  $O_s = \hat{O}_s \otimes \mathbb{I}_{X \setminus s}$ , where  $\hat{O}_s$  is some operator living in the Hilbert space of  $s$ .

Now, if the state of  $X$ ,  $\rho_X$ , is g-locally thermal at each  $s$ , with uniform g-local temperature  $T$ , then

$$\begin{aligned} \langle O \rangle &:= \text{Tr}_X [O \rho_X] \\ &= \sum_s \text{Tr}_X [(\hat{O}_s \otimes \mathbb{I}_{X \setminus s}) \rho_X] \\ &= \sum_s \text{Tr}_s [\hat{O}_s \rho_s] \\ &\stackrel{(*)}{=} \sum_s \text{Tr}_s [\hat{O}_s \text{Tr}_{X \setminus s} [\tau(T, H_X)]] \\ &= \sum_s \text{Tr}_X [(\hat{O}_s \otimes \mathbb{I}_{X \setminus s}) \tau(T, H_X)] \\ &= \text{Tr}_X [O \tau(T, H_X)], \end{aligned} \quad (\text{B2})$$

where in step (\*) the g-locality condition (2) was used.

This in particular means that, if  $H_X$  is local, then the effective canonical temperature  $T_X^{\text{eff,can}}$  of  $X$ , defined in Eq. (8), coincides with  $T$ . Indeed, in view of Eqs. (B2), one has  $\text{Tr}[\rho_X H_X] = \text{Tr}[H_X \tau(T, H_X)]$ . Moreover, if we define the “g-local” heat capacity of  $X$  as  $d\text{Tr}[H_X \rho_X]/dT$ , then it will be equal to the heat capacity of  $X$  if it were in a global thermal state at temperature  $T$ .

Note that, in some cases, it might happen that  $\rho_X$  is g-locally thermal also at small, but spatially *delocalized* subsystems containing at most  $k$  sites. Then, the equality  $T_X^{\text{eff,can}} = T_X^{\text{eff}}$  will hold even if  $H_X$  is a long-range, but at most  $k$ -body, interacting Hamiltonian.

Finally, we note that the effective canonical temperature  $T_X^{\text{eff,can}}$  has found some use in nonequilibrium thermodynamics [110–112], and the equality  $T_X^{\text{eff,can}} = T_X^{\text{eff}}$  for g-locally thermal systems provides  $T_X^{\text{eff,can}}$  with an additional thermodynamic meaning.

## APPENDIX C: A SUMMARY OF HARMONIC SYSTEMS

As described in Sec. III, our model system is a harmonic lattice. Namely, it is a collection of linearly coupled oscillators, so all the Hamiltonians are quadratic.

The tools for simulating and calculating many physical and information-theoretical quantities for such systems are well-known and thoroughly described in, e.g., Refs. [56–58]. Here we will give a brief account of the main notions and formulas necessary for our purposes.

The position and momentum coordinates of a system of  $N$  oscillators are conveniently collected into a column vector in the phase space

$$\mathbf{x} = \begin{pmatrix} \mathbf{q} \\ \mathbf{p} \end{pmatrix}, \quad (\text{C1})$$

with a total of  $2N$  components

$$\mathbf{q} = (q_1, \dots, q_N)^T, \quad \mathbf{p} = (p_1, \dots, p_N)^T.$$

We call this phase-space basis the “q-p” basis. In this basis, and in units where  $\hbar = 1$ , the canonical commutation relations are written as

$$[x_k, x_j] = i\Upsilon_{k,j}, \quad (\text{C2})$$

where the antisymmetric matrix  $\Upsilon$  has the symplectic form:

$$\Upsilon = \begin{pmatrix} 0 & \mathbb{I} \\ -\mathbb{I} & 0 \end{pmatrix}, \quad (\text{C3})$$

with  $\mathbb{I}$  being the  $N \times N$  identity matrix and  $0$  the  $N \times N$  zero matrix. (A relation similar to (C2) applies in classical mechanics, but with the Poisson bracket instead of the commutator.)

In terms of the phase-space coordinates  $\mathbf{x}$ , the Hamiltonian is a quadratic form

$$H = \frac{1}{2} \mathbf{x}^T F \mathbf{x}, \quad (\text{C4})$$

where we call the symmetric matrix  $F$  the “Hamiltonian matrix.” When there is no momentum–momentum coupling in the system,  $F$  will take the form

$$F = V \oplus \mathbb{I}, \quad (\text{C5})$$

where  $V$  corresponds to the “potential energy” part of the Hamiltonian, and the identity  $\mathbb{I}$  specifies the kinetic energy (after scaling out the oscillator masses).

Two harmonic systems  $A$  and  $B$  can be combined by forming the direct sum of their phase spaces, with the joint Hamiltonian matrix

$$F_{AB} = V_{AB} \oplus \mathbb{I}_{AB}, \quad (\text{C6})$$

where

$$V_{AB} = V_A \oplus V_B + V_{\text{int}}. \quad (\text{C7})$$

Here the interaction potential  $V_{\text{int}}$  represents  $H_{\text{int}}$  that couples  $A$  and  $B$  [see, e.g., Eq. (11)].

Due to a theorem by Williamson [113], any Hamiltonian matrix can be symplectically diagonalized. Namely,

there exists a symplectic transformation matrix  $S$  such that

$$S^T F S = \Omega \oplus \Omega, \quad (\text{C8})$$

where the diagonal matrix  $\Omega = \text{diag}(\Omega_1, \dots, \Omega_N)$  collects the normal mode frequencies of the system. Recall that symplectic is any matrix that leaves the canonical commutation relation (C2) invariant:  $S^T \Upsilon S = \Upsilon$ .

The same matrix  $S$  switches from the q-p basis to the normal mode basis:

$$\mathbf{x} = S \mathbf{X}, \quad (\text{C9})$$

where  $\mathbf{X} = (Q_1, \dots, Q_N, P_1, \dots, P_N)^T$  collects the positions and momenta of the normal modes. In the normal-mode basis, the Hamiltonian is a sum of non-interacting oscillators:

$$H = \sum_j \Omega_j \left[ \frac{Q_j^2}{2} + \frac{P_j^2}{2} \right]. \quad (\text{C10})$$

The initial state  $\rho(0)$  (12) is a tensor product of Gibbs states of quadratic Hamiltonians; therefore, it is Gaussian. Hence, there is no net displacement of the phase-space coordinates,  $\langle \mathbf{x} \rangle_t := \text{Tr}[\rho(t) \mathbf{x}] = 0$ , and, since the Hamiltonian is quadratic at all times, the state  $\rho(t)$  also remains Gaussian at all times [58].

Gaussian states are uniquely determined by the covariance matrix [58]

$$\sigma_{jk} = \frac{1}{2} \text{Tr}[\rho(x_j x_k + x_k x_j)], \quad (\text{C11})$$

where the curly brackets denote the anticommutator. Conveniently, the covariance matrix of any subsystem (in our case, it can be  $A$  or  $B$  or some small subsystem of sites) is simply the corresponding sub-block of  $\sigma$ , which determines its reduced state.

Whenever the system is in a Gibbs state (i.e.,  $\rho = \tau(T, H)$  (1)), the covariance matrix in the normal-mode basis,

$$\Sigma_{jk} = \frac{1}{2} \text{Tr}[\tau(T, H)(X_j X_k + X_k X_j)], \quad (\text{C12})$$

is diagonal and given by [58]

$$\Sigma = R \oplus R, \quad (\text{C13})$$

where  $R = \text{diag}(R_1, \dots, R_N)$ , with

$$R_j = \frac{1}{2} \coth \frac{\Omega_j}{2T}. \quad (\text{C14})$$

Due to Eq. (C9), the covariance matrix in the “original” q-p basis  $x$  is then

$$\sigma = S \Sigma S^T. \quad (\text{C15})$$

Noting that the covariance matrix for a tensor product  $\rho_A \otimes \rho_B$  is a direct sum,  $\sigma_A \oplus \sigma_B$ , we can thus construct the covariance matrix of the initial state (12).

As for calculating the dynamics of the system, it can be derived immediately from the Heisenberg equations of motion for  $\mathbf{x}$  that the evolution of the covariance matrix under a quadratic Hamiltonian is a symplectic transformation [58, 114]:

$$\sigma(t) = \mathcal{E}(t)\sigma(0)\mathcal{E}(t)^T, \quad (\text{C16})$$

where  $\mathcal{E}(t)$  is a symplectic matrix. Moreover,  $\mathcal{E}(t)$  is explicitly expressed through the matrix  $F$  (C4) [115, 116]. When the Hamiltonian is time-independent,  $F$  is constant and

$$\mathcal{E}(t) = e^{\Upsilon Ft}. \quad (\text{C17})$$

Furthermore, to find effective g-local temperatures through Eq. (5), we need to calculate the fidelity (7). For two  $N$ -mode Gaussian states  $\rho_1$  and  $\rho_2$  with respective covariance matrices  $\sigma_1$  and  $\sigma_2$  and identical average coordinates (which are zero in our case), the fidelity is given by [109]

$$\mathcal{F}(\rho_1, \rho_2) = \sqrt[4]{\frac{M}{\det(\sigma_1 + \sigma_2)}}, \quad (\text{C18})$$

where

$$M = \det \left[ 2 \left( \sqrt{\mathbb{I} + \frac{1}{4}(C\Upsilon)^{-2} + \mathbb{I}} \right) C \right], \quad (\text{C19})$$

with  $\mathbb{I}$  and  $\Upsilon$  being the  $(2N) \times (2N)$  identity matrix and the symplectic form [Eq. (C3)], respectively. The matrix  $C$  is defined as

$$C = -\Upsilon(\sigma_1 + \sigma_2)^{-1} \left( \frac{\Upsilon}{4} + \sigma_2 \Upsilon \sigma_1 \right). \quad (\text{C20})$$

Lastly, let us find the generalized inverse temperatures  $\beta_\kappa$  in the GGE for harmonic systems. These are determined from Eq. (15). Since all the charges  $h_\kappa$  live in non-overlapping Hilbert spaces, we have

$$\text{Tr} [h_\kappa \rho_{AB}^{\text{GGE}}] = \frac{\text{Tr} [h_\kappa e^{-\beta_\kappa h_\kappa}]}{\text{Tr} [e^{-\beta_\kappa h_\kappa}]} = \frac{\Omega_\kappa}{2} \coth \frac{\beta_\kappa \Omega_\kappa}{2}.$$

Thus, equating this to  $\langle h_\kappa \rangle = \text{Tr} [h_\kappa \rho_{AB}(0)]$ , we find

$$\beta_\kappa = \frac{2}{\Omega_\kappa} \text{arctanh} \frac{\Omega_\kappa}{2 \langle h_\kappa \rangle}. \quad (\text{C21})$$

#### APPENDIX D: G-LOCAL THERMALITY FOR EDGE-EDGE COUPLED LATTICES

EE coupling is present when the interaction Hamiltonian is of the form

$$H_{\text{int}}^{(\text{EE})} = \lambda \sum_{\nu \in \text{edge}} q_{A,\nu} q_{B,\nu}, \quad (\text{D1})$$

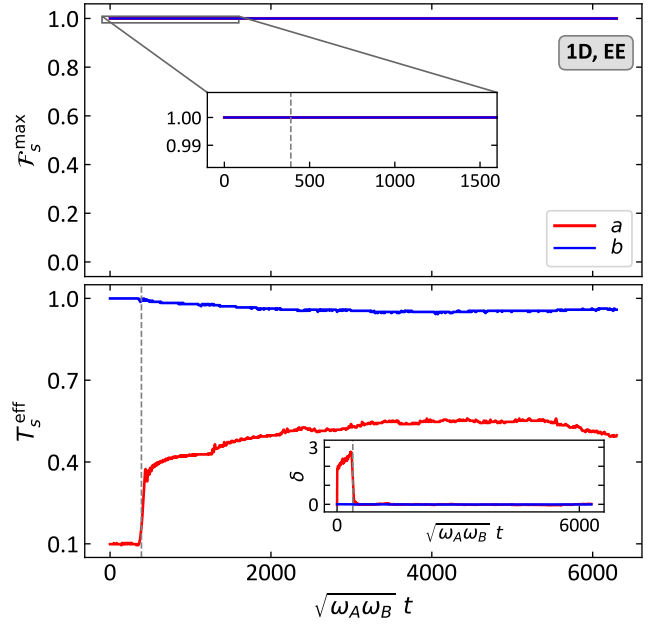


FIG. 11: (**G-local thermality of  $A$  at  $a$  and  $B$  at  $b$ .**) Similarly to Fig. 4, the **top panel** shows the fidelity  $\mathcal{F}_s^{\text{max}}$  (7) of  $A$  at  $s = a$  (red) and of  $B$  at  $s = b$  (blue) as a function of time  $t$ . For each  $X$ , the single-site subsystem  $s$  is located at the center of the lattice  $X$ .  $A$  and  $B$  are connected at  $\nu = 1$ . The inset zooms into the fidelity at early times. The fidelities remain very close to 1 (smallest  $\mathcal{F}_s^{\text{max}}$  being 0.999979), indicating that both  $A$  and  $B$  are g-locally thermal at  $a$  and  $b$ , respectively, with extremely good precision *at all times* during the evolution. The **bottom panel** shows the corresponding effective temperatures  $T_s^{\text{eff}}$  (5). The inset is for  $\delta$ —the relative discrepancy between the effective g-local and canonical temperatures. It is large in the transient regime, signalling a significant temperature gradient in the system (cf. Fig. 12). This plot is for  $A$  and  $B$  having only nearest-neighbor interactions within them ( $\alpha = \infty$ ). All other parameters are the same as in Fig. 4. The vertical dashed line indicates the instance at which Fig. 12 is plotted.

where  $\nu$  runs over the sites located on the interacting edge of each lattice (see left column of Fig. 2 for an illustration).

For example, when  $A$  and  $B$  are 1D, the edge consists of a single site. For such a configuration with  $A$  and  $B$  featuring nearest-neighbor interactions, the dynamics of the fidelity  $\mathcal{F}_s^{\text{max}}$  and effective g-local temperature  $T_s^{\text{eff}}$  of a single-site subsystem  $s$  located at the center of  $X$  is plotted in Fig. 11. Similarly to the case of FB coupling discussed in Sec. IV, we see that  $s$  remains g-locally thermal at all times with a good approximation.

We also notice on the bottom panel of Fig. 11 that the effective temperature of  $s$  remains unchanged for some time. This happens because the speed of sound in each



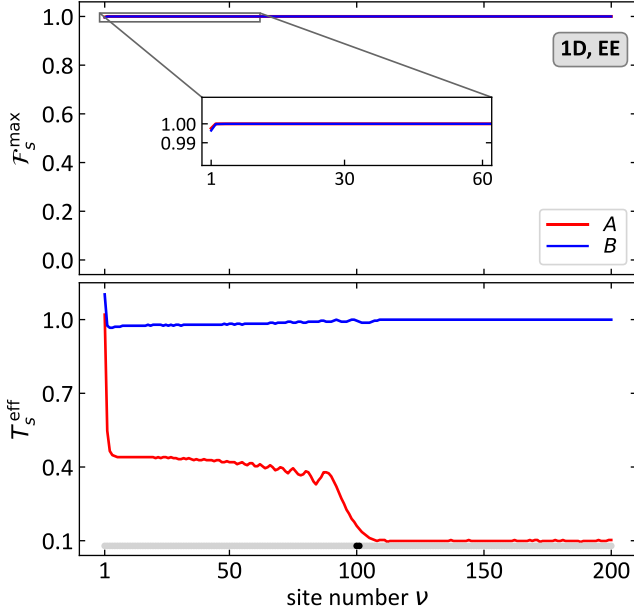


FIG. 12: **(G-local thermality with site number  $\nu$ .)** Similarly to Fig. 6, the **top panel** plots the fidelity  $\mathcal{F}_s^{\max}$  (7) of  $A$  at single-site subsystem  $s = a$  (red) and of  $B$  at  $s = b$  (blue), respectively, and the **bottom panel** shows the corresponding effective temperatures  $T_s^{\text{eff}}$  (5) as a function of the site number  $\nu$ . Here  $\nu$  labels *all* single-site subsystems  $s$  in  $X$ , with  $\nu = 1, \dots, N$ . One sees that the fidelities  $\mathcal{F}_s^{\max}$  are very close to 1 for all  $\nu$  (the smallest  $\mathcal{F}_s^{\max}$  being 0.996439). However, in contrast to the [1D, FB] case shown in Fig. 6, the g-local temperatures  $T_s^{\text{eff}}$  *change* with  $s$ —there is a (g-local) temperature gradient in the system. The “slider” (black dot) at the bottom indicates the position of the subsystem  $s$  in  $X$  at which Fig. 11 is plotted. Here,  $\sqrt{\omega_A \omega_B} t_0 \approx 389.71$ , and all other parameters are as in Fig. 11.

system is finite, and therefore it takes a finite amount of time until the perturbation caused by switching on the coupling at the edge to reach the center of the chain (where  $s$  is).

For this very reason, there is also a temperature gradient within each lattice  $X$  in the transient regime, before the total system equilibrates. A snapshot of that is presented in Fig. 12, where the fidelity  $\mathcal{F}_s^{\max}$  and effective g-local temperature  $T_s^{\text{eff}}$  are plotted as a function of the position of a single-site subsystem  $s$  that slides along the chain (just like in Fig. 6). Here we see that, while all  $s$  are g-locally thermal with excellent approximation, their temperature now depends on the position of  $s$ . Due to this gradient, the effective canonical temperature (8) becomes inadequate, as is emphasized in the inset of the bottom panel of Fig. 11.

Expectedly, at those times when there is a temperature gradient in the lattices, the decay of  $\mathcal{F}_s^{\max}$  with  $N_s$  is faster as compared with the FB case. Moreover, even small (e.g.,  $N_s = 2$ ) but delocalized subsystems  $s$  (i.e.,

when  $s = \{\nu_1, \nu_2\}$  with, e.g.,  $\nu_1 = 50$  and  $\nu_2 = 150$ ), are not g-locally thermal anymore. This contrasts the [1D, FB] and [2D, FB] cases, where all small subsystems, localized or not, are g-locally thermal with good approximation.

## APPENDIX E: NUMERICAL DEMONSTRATION OF THE MAIN RESULT

In this section, we numerically demonstrate the validity of our main result laid out in Sec. IV (and illustrated in Fig. 3). It states that g-local thermality of  $A$  and  $B$  is guaranteed *at all times, including during the transient*, whenever all local observables of  $AB$  equilibrate dynamically at long times.

We will first describe the parameter space and then discuss the relevant figures of merit and show pertinent results of our simulations.

### 1. Parameterization

A natural dimensionless parametrization of the system and its dynamics can be achieved as follows. First of all, we recall that we work in the natural units where  $\hbar = k_B = 1$  and the masses of all the oscillators are set to 1. Therefore, the transformation  $\tilde{q} = q/\sqrt{\omega}$ ,  $\tilde{p} = p/\sqrt{\omega}$  will render  $\tilde{q}$  and  $\tilde{p}$  dimensionless while preserving the canonical commutation relations. In these terms,

$$H_X = \omega_X h_X(\tilde{q}_\nu, \tilde{p}_\nu, \tilde{g}_X, \alpha), \quad (\text{E1})$$

where the dimensionless operator function  $h_X$  of the dimensionless quantities  $(\tilde{q}_\nu, \tilde{p}_\nu, \tilde{g}_X, \alpha)$ , with

$$\tilde{g}_X := g_X/\omega_X^2, \quad (\text{E2})$$

is given by

$$h_X = \frac{1}{2} \sum_\nu (\tilde{q}_\nu^2 + \tilde{p}_\nu^2) + \sum_{\nu \neq \nu'} \tilde{G}_X^{\nu, \nu'} \tilde{q}_{X, \nu} \tilde{q}_{X, \nu'}. \quad (\text{E3})$$

Here, by natural extension of Eq. (10),

$$\tilde{G}_X^{\nu, \nu'} := \frac{\tilde{g}_X}{\text{dist}(\nu, \nu')^\alpha}. \quad (\text{E4})$$

Introducing the dimensionless lattice–lattice coupling

$$\tilde{\lambda} := \lambda/(\omega_A \omega_B), \quad (\text{E5})$$

and

$$\mu := \sqrt{\omega_A/\omega_B}, \quad (\text{E6})$$

we obtain the total Hamiltonian

$$H_{\text{tot}} = \sqrt{\omega_A \omega_B} h_{\text{tot}}, \quad (\text{E7})$$

where, for e.g. the FB coupling, the dimensionless operator  $h_{\text{tot}}$  is

$$h_{\text{tot}} = \mu h_A + \mu^{-1} h_B + \tilde{\lambda} \sum_\nu \tilde{q}_{A, \nu} \tilde{q}_{B, \nu}. \quad (\text{E8})$$

As mentioned in Sec. III, in the 5-dimensional system-parameter space with coordinates  $(\mu, \alpha, \tilde{\lambda}, \tilde{g}_A, \tilde{g}_B)$ , the set of allowed system parameters is determined by the condition that the operator  $h_{\text{tot}}$  is unbounded from below.

Lastly, the evolution in dimensionless time

$$\tilde{t} := t\sqrt{\omega_A\omega_B} \quad (\text{E9})$$

is generated by

$$U = e^{-i\tilde{t}h_{\text{tot}}}. \quad (\text{E10})$$

And defining the dimensionless temperatures as

$$\tilde{T}_X := T_X/\omega_X, \quad (\text{E11})$$

we can express the initial state (12) in terms of dimensionless quantities:

$$\rho_{AB}(0) \propto e^{-h_A/\tilde{T}_A} \otimes e^{-h_B/\tilde{T}_B}. \quad (\text{E12})$$

## 2. Relevant quantities and data

Although we formulated our all-time g-local thermality result in a “discrete” true–false language (see Fig. 3), there is more quantitative structure to the dependence of the degree of g-local thermality on the degree of long-time equilibration. To properly showcase this relationship, we need a quantification of both phenomena.

First of all, we pick a long enough time interval  $[0, \tilde{t}_m]$  over which we observe the system. Then, since we already have a well-defined measure of g-local thermality at an instant of time  $\tilde{t}$  and subsystem  $s$ ,  $\mathcal{F}_s^{\text{max}}(\tilde{t})$ , we use it to introduce a measure of all-time (AT) g-local thermality at  $s$  defined as

$$\mathcal{F}_s^{\text{AT}} = \min_{\tilde{t} \in [0, \tilde{t}_m]} \mathcal{F}_s^{\text{max}}(\tilde{t}). \quad (\text{E13})$$

To quantify the degree to which the system locally equilibrates as per the definition in Sec. V, we will employ the fact that, if equilibration occurs, then it is described by the GGE in the thermodynamic limit (see Sec. V). The main quantifier here is the longest “equilibrium interval” during the  $[0, \tilde{t}_m]$  period. By an equilibrium interval we mean any  $[\tilde{t}_i^{\text{eq}}, \tilde{t}_f^{\text{eq}}]$  such that  $\mathcal{D}[\rho_s(\tilde{t}), \rho_s^{\text{GGE}}] \leq \epsilon \forall \tilde{t} \in [\tilde{t}_i^{\text{eq}}, \tilde{t}_f^{\text{eq}}]$ . The figure of merit we will use is the ratio of the longest equilibrium interval,

$$\tau_s^{\text{eq}} := \max_{[\tilde{t}_i^{\text{eq}}, \tilde{t}_f^{\text{eq}}] \subset [0, \tilde{t}_m]} (\tilde{t}_f^{\text{eq}} - \tilde{t}_i^{\text{eq}}) \quad (\text{E14})$$

to the total duration of observation:

$$r_s^{\text{eq}} = \frac{\tau_s^{\text{eq}}}{\tilde{t}_m}. \quad (\text{E15})$$

In parallel with  $r_s^{\text{eq}}$ , we will use the average distance from equilibrium,

$$\langle \mathcal{D}_s \rangle = \frac{1}{\tilde{t}_m} \int_0^{\tilde{t}_m} d\tilde{t} \mathcal{D}[\rho_s(\tilde{t}), \rho_s^{\text{GGE}}], \quad (\text{E16})$$

to quantify local equilibration.

The quantity  $\langle \mathcal{D}_s \rangle$  cannot be used alone to “measure” equilibration, as even a very small value of  $\langle \mathcal{D}_s \rangle$  does not exclude frequent  $\epsilon$ -surpassing peaks of  $\mathcal{D}[\rho_s(\tilde{t}), \rho_s^{\text{GGE}}]$ . Similarly, used alone,  $r_s^{\text{eq}}$  indicates the time  $\mathcal{D}_s$  uninterruptedly spends under  $\epsilon$ , but does not tell us how much lower than  $\epsilon$  it typically gets. So, although  $r_s^{\text{eq}}$  and  $\langle \mathcal{D}_s \rangle$  are not independent (e.g., if  $r_s^{\text{eq}} = 1$ , then necessarily  $\langle \mathcal{D}_s \rangle \leq \epsilon$ ), only when considering them together does one get a complete picture of how well  $AB$  locally equilibrates at  $s$ —one needs a small  $\langle \mathcal{D}_s \rangle$  and a large  $r_s^{\text{eq}}$  to ensure equilibration.

Regarding the choice of  $\tilde{t}_m$ , we note that, although verifying equilibration is in general an undecidable problem [117], the situation in quadratic harmonic systems is more predictable. Indeed, as discussed in Sec. V, if equilibration occurs, then the equilibrium is described by the GGE. Moreover, it was shown in Ref. [74] that, if the interactions in the system are of short range, then the equilibration time does not depend on the system size and the recurrence time grows linearly with the size. For systems with long-range interactions, our numerical experiments show that the pattern is similar—if the system equilibrates, it does so relatively quickly; and if it does not, then local states show no tendency to converge at long times. For the plots in Figs. 13–15, we found  $\tilde{t}_m = 10000$  to be sufficiently long, yet not too long for recurrences to significantly affect the picture.

In terms of the above-introduced quantities, the claim in our main result is as follows (see Fig. 3 for a recap). If  $r_s^{\text{eq}}$  is small **or**  $\langle \mathcal{D}_s \rangle$  is large (i.e., poor equilibration) then  $\mathcal{F}_s^{\text{AT}}$  can be anything. If  $r_s^{\text{eq}}$  is close to 1 **and**  $\langle \mathcal{D}_s \rangle$  is small (i.e., good equilibration), then  $\mathcal{F}_s^{\text{AT}}$  has to be close to 1.

This is indeed what we see numerically. We have explored the full parameter range by both randomly sampling the parameters  $(\mu, \alpha, \tilde{\lambda}, \tilde{g}_A, \tilde{g}_B, \tilde{T}_A, \tilde{T}_B)$  and deliberately choosing values at the boundaries of the set of allowed parameters (determined by the condition that the total Hamiltonian is nonnegative; see Appendix E1).

Since the parameter space is 7-dimensional (not counting  $N_A, N_B$ , and the configuration of lattice–lattice interaction), and therefore impossible to draw, we will present our results in two-dimensional cross-sections.

In our numerical experiments, we found that there are three “dangerous” parameter regimes. First is strong  $A/B$  frequency imbalance:  $\mu \ll 1$  or  $\mu \gg 1$ . The other parameter that has a significant effect on g-local-thermality–equilibration relation is  $\alpha$ —the range of intra-lattice interactions. Indeed, as we will see in Appendix F, canonical-typicality–based results become inapplicable for small values of  $\alpha$ , making the regime of small  $\alpha$ ’s also dangerous. The third is the regime of strong lattice–lattice coupling, which also bears the potential to be dangerous as both  $A$  and  $B$  lose their dynamic individuality when  $\tilde{\lambda}$  is large, especially in the FB coupling configuration. Therefore, our emphasis will be on cross-sections of  $\mu, \alpha$ , and  $\tilde{\lambda}$ . Note that large  $\tilde{\lambda}$  means that  $|\tilde{\lambda}|$  is close

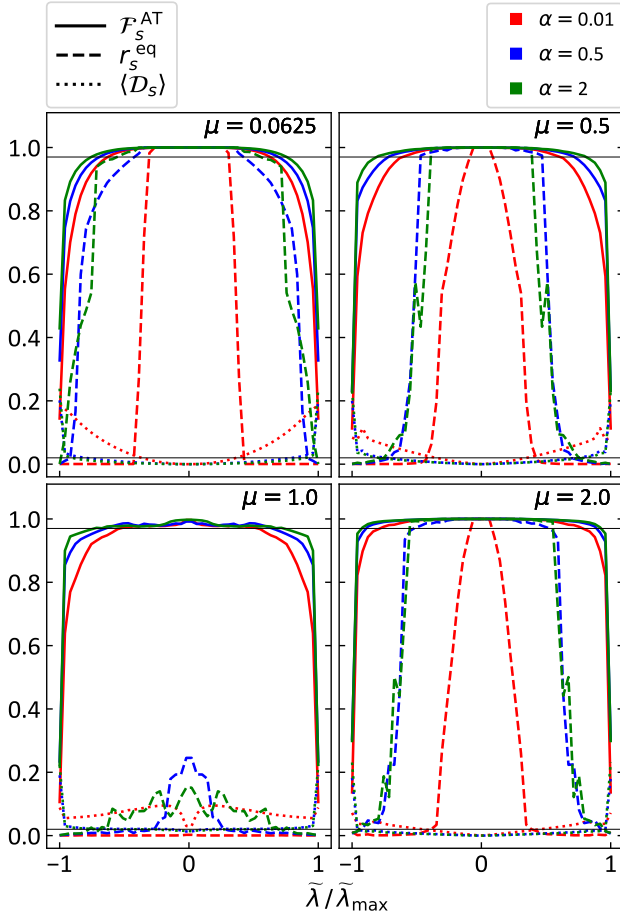


FIG. 13: (Degrees of all-time g-local thermality and long-time equilibration vs  $\tilde{\lambda}$ .) Each panel shows  $\mathcal{F}_s^{\text{AT}}$  (solid line),  $r_s^{\text{eq}}$  (dashed line), and  $\langle \mathcal{D}_s \rangle$  (dotted line) as functions of  $\tilde{\lambda}$ . Different colors correspond to different values of  $\alpha$ . The upper horizontal line is at 0.97 and represents the threshold value of  $\mathcal{F}_s^{\text{AT}}$  above which we say that the system is g-locally thermal at all times. The lower horizontal line is the  $\epsilon = 0.02$  threshold for  $\langle \mathcal{D}_s \rangle$ . The configuration is [1D, FB], and the plots are for the central two-node subsystem of  $A$ . All the other parameters are  $N_A = N_B = 200$ ,  $\tilde{g}_A = 0.2$ ,  $\tilde{g}_A = 0.3$ ,  $\tilde{T}_A = 0.1$ ,  $\tilde{T}_B = 1$ . The  $\mu = 1$  ( $\omega_A = \omega_B$ ) case is peculiar in that the equal frequencies result in resonant oscillations that give rise to periodic spikes in  $\mathcal{D}[\rho_s(t), \rho_s^{\text{GGE}}]$ , resulting in poor equilibration. The system experiences all-time g-local thermality to a good extent nonetheless. Viewing the plot from  $\tilde{\lambda} = 0$ , we see that the quality of equilibration deteriorates much faster than the degree of all-time g-local thermality as  $\tilde{\lambda}$  approaches  $\pm\tilde{\lambda}_{\text{max}}$ —the maximal value of  $|\tilde{\lambda}|$  for which  $H_{\text{tot}}$  is bounded from below.

to  $\tilde{\lambda}_{\text{max}}$ , which is the maximal value of  $|\tilde{\lambda}|$  (with all other parameters fixed) for which  $H_{\text{tot}}$  is bounded from below.

The most insight is provided by Fig. 13, where we plot the degrees of all-time g-local thermality ( $\mathcal{F}_s^{\text{AT}}$ ) and

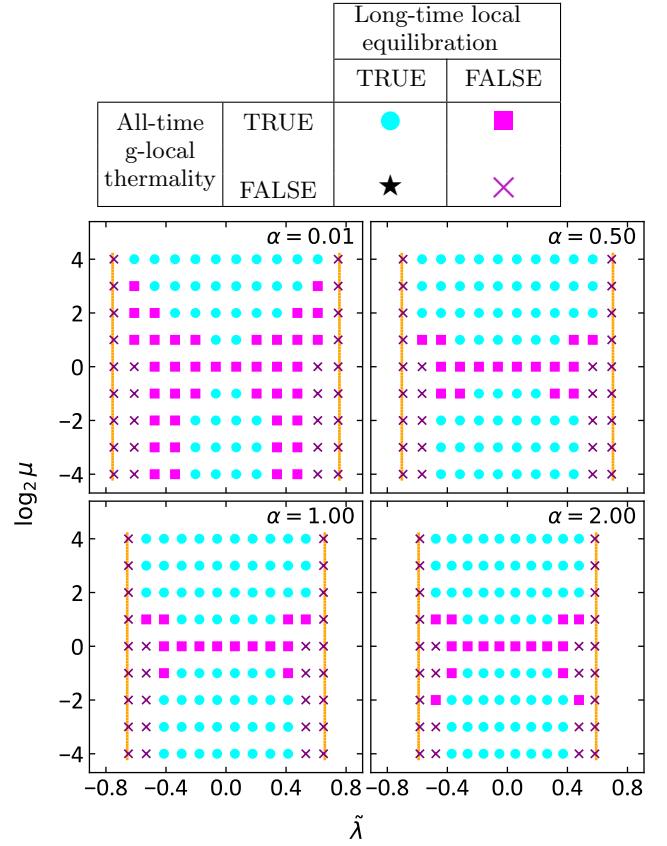


FIG. 14: (All-time g-local thermality and long-time local equilibration vs  $\tilde{\lambda}$  and  $\mu$ .) Each panel shows whether or not all-time g-local thermality and long-time equilibration occur, as per the color- and shape-coding in the table, as a function of  $\tilde{\lambda}$  and  $\mu$ . The panels are for four different values of  $\alpha$ , with all other parameters fixed to the same values as in Fig. 13. The orange lines are at  $\pm\tilde{\lambda}_{\text{max}}$ , marking the boundary of the set of all  $(\tilde{\lambda}, \mu)$  for which  $H_{\text{tot}}$  is bounded from below. Here the TRUE-threshold for all-time g-local thermality is chosen to be  $\mathcal{F}_s^{\text{AT}} \geq 0.97$  for all subsystems  $s$  of size two. For long-time equilibration, the TRUE-threshold is  $\min_{|s|=2} r_s^{\text{eq}} \geq 0.8$  and  $\max_{|s|=2} \langle \mathcal{D}_s \rangle \leq \epsilon = 0.02$ . We see that all combinations occur except the ★, in accordance with the claim in the main text; see also Fig. 3. **The table** shows the shape- and color-coding of the four logical possibilities for observing or not observing all-time g-local thermality and long-time local equilibration used in the plot.

equilibration ( $r_s^{\text{eq}}$  and  $\langle \mathcal{D}_s \rangle$ ) as functions of  $\tilde{\lambda}$ , for different (extremal and not) values of  $\alpha$  and  $\mu$ . There we see that the quality of equilibration deteriorates significantly faster than the degree of all-time g-local thermality as  $|\tilde{\lambda}|$  approaches its maximum ( $\tilde{\lambda}_{\text{max}}$ ). This confirms our claim and, in a way, makes the relation between all-time g-local thermality and long-time equilibration more quantitative.

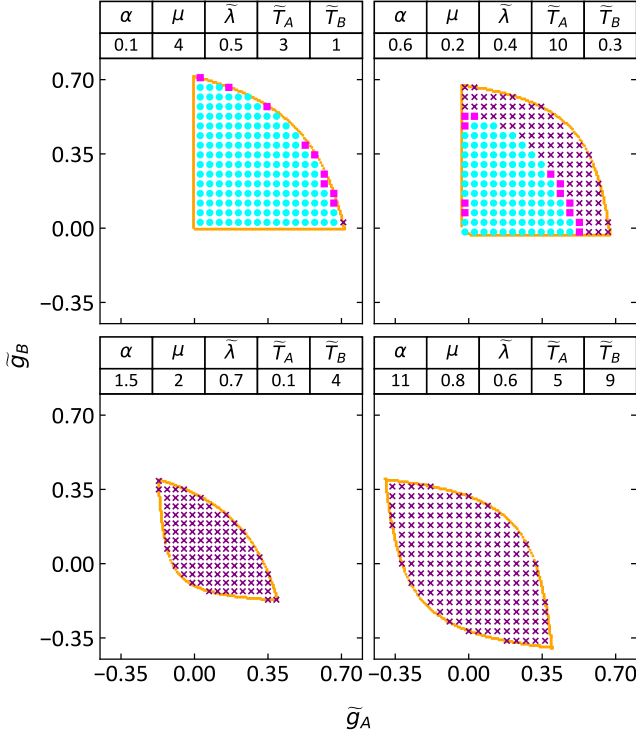


FIG. 15: (All-time g-local thermality and long-time local equilibration vs  $\tilde{g}_A$  and  $\tilde{g}_B$ .) Each panel shows whether or not all-time g-local thermality and long-time equilibration occur, as per the color- and shape-coding in the table in Fig. 14, as a function of  $\tilde{g}_A$  and  $\tilde{g}_B$ . The panels are for four different sets of parameters  $(\alpha, \mu, \tilde{\lambda}, \tilde{T}_A, \tilde{T}_B)$  shown on top of each panel. As previously,  $N_A = N_B = 200$  and the configuration is [1D, FB]. On each panel, the orange border outlines the set of all  $(\tilde{g}_A, \tilde{g}_B)$  such that  $H_{\text{tot}}$  is bounded from below. As in Fig. 14, here the TRUE-threshold for all-time g-local thermality is  $\min_{|s|=2} \mathcal{F}_s^{\text{AT}} \geq 0.97$ , and for long-time equilibration, the TRUE-threshold is  $\min_{|s|=2} \tau_s^{\text{eq}} \geq 0.8$  and  $\max_{|s|=2} \langle D_s \rangle \leq \epsilon = 0.02$ . We see that all combinations occur except the  $\star$ , in accordance with the claim illustrated in Fig. 3. The lack of all-time g-local thermality and equilibration in two bottom panels is consistent with Fig. 13: in both panels,  $\tilde{\lambda}/\tilde{\lambda}_{\text{max}}$  is close to 1.

A different cross-section of the  $(\mu, \alpha, \tilde{\lambda})$  subset is presented in Fig. 14. There we plot all-time g-local thermality and long-time local equilibration in a discrete fashion: occurs (TRUE) or does not occur (FALSE). The four logical possibilities are presented in the table in Fig. 14, with corresponding color- and shape-coding. Now, the claim of our main result, as formulated in Sec. IV and summarized in Fig. 3, is that the combination [all-time g-local thermality = FALSE] and [long-time local equilibration = TRUE], encoded as  $\star$ , never occurs. And indeed, we

see no  $\star$  in Fig. 14.

Figure 15 is another TRUE-FALSE plot, this time across four  $(\tilde{g}_A, \tilde{g}_B)$  planes, each corresponding to a panel of the plot. The values of the parameters fixing the planes are presented above the panels. In the top left panel, we have  $A$  with much larger initial energy and heat capacity ( $\omega_A = 16\omega_B$  and  $T_A = 48T_B$ ), so, expectedly, the evolution does not perturb it much, so its g-local thermality is largely maintained even at the edge of the parameter space. On the top right panel,  $A$  has a much smaller heat capacity than  $B$  ( $\omega_A = \omega_B/25$ ) and starts at a similar temperature with  $B$  ( $T_A \approx 1.33T_B$ ), so we see more diversity of options. In two bottom panels, the respective  $\tilde{\lambda}$ 's are close to their maximal values, so, as could be anticipated from Fig. 13, we observe that neither all-time g-local thermality nor long-time local equilibration occur to a high enough degree.

We observe the picture described above over all cross-sections of the parameter set, for all configurations and spatial dimensions. We take this as a compelling numerical proof of our main result.

## APPENDIX F: COMPARISON WITH ENSEMBLE EQUIVALENCE

By the stronger equivalence of ensembles, we mean Proposition 2 in Ref. [50]. In a slightly simplified form derived in Ref. [55] (Lemma 2), it states the following. Say,  $X$  is a  $d$ -dimensional (hyper)cubic lattice with  $N = n^d$  sites. Each site contains a quantum system described by a finite-dimensional Hilbert space, with the dimension being the same for all sites. The Hamiltonian is of finite range (i.e., local, as per the definition in Appendix B):  $H_X = \sum_{\nu \in X} \mathfrak{h}_\nu$ , with  $\mathfrak{h}_\nu$  acting only on sites  $\nu'$  with  $\text{dist}(\nu, \nu') \leq k$ . Now, let  $\tau_X$  be a state with exponentially decaying correlations and fix some  $0 < c < 1/(d+2)$ . If

$$S(\rho_X \| \tau_X) = o(N^{\frac{1-c(d+2)}{d+1}}), \quad (\text{F1})$$

where  $S(\rho \| \tau) := \text{Tr}[\rho(\ln \rho - \ln \tau)]$  is the relative entropy, then [50, 55]

$$\mathbb{E}_{s \in C_l} \|\rho_s - \tau_s\|_1 = O(N^{-c/2}), \quad (\text{F2})$$

where  $\|\mathfrak{D}\|_1 := \text{Tr} \sqrt{\mathfrak{D}^T \mathfrak{D}}$  is the trace norm,  $C_l$  is the set of all sub-hypercubes  $s$  of  $X$  with side length

$$l = o(n^{\frac{1-c}{d+1}}), \quad (\text{F3})$$

and  $\mathbb{E}_{s \in C_l}$  denotes arithmetic averaging over  $C_l$ . Namely,

$$\mathbb{E}_{s \in C_l} \|\rho_s - \tau_s\|_1 := \frac{1}{K_l} \sum_{s \in C_l} \|\rho_s - \tau_s\|_1, \quad (\text{F4})$$

where  $K_l$  is the size of  $C_l$  (i.e., the amount of sub-hypercubes  $s$  in it). Here, the big- $O$  and small- $o$  are



as per the standard asymptotic notation, and, as in the main text,  $\rho_s := \text{Tr}_{X \setminus s}[\rho_X]$ .

In simple terms, this lemma means that, if  $\tau_X$  has exponentially decaying correlations, and  $\rho_X$  is not very far from it in terms of the relative entropy [Eq. (F1)], then  $\rho_X$  is locally close to  $\tau_X$ , in trace norm, for almost all small subsystems [Eq. (F2)]. Here, small is any subsystem the diameter of which is  $o(n^{\frac{1-c}{d+1}})$  [Eq. (F3)]; of course, any fixed size is  $o(n^{\frac{1-c}{d+1}})$  in the thermodynamic limit.

To translate Eq. (F2) into a statement about the Bures distance, note that, in view of the Fuchs–van de Graaf inequality [118],  $\mathcal{D}[\rho, \tau]^2 \leq \|\rho - \tau\|_1$ . Therefore,

$$\begin{aligned} \mathbb{E}_{s \in C_l} \mathcal{D}[\rho_s, \tau_s] &= \frac{1}{K_l} \sum_{s \in C_l} 1 \cdot \mathcal{D}[\rho_s, \tau_s] \\ &\stackrel{(*)}{\leq} \frac{1}{K_l} \sqrt{\sum_{s \in C_l} 1^2} \sqrt{\sum_{s \in C_l} \mathcal{D}[\rho_s, \tau_s]^2} \\ &\leq \sqrt{\frac{1}{K_l} \sum_{s \in C_l} \|\rho_s - \tau_s\|_1}, \end{aligned}$$

where the step (\*) is due to the Cauchy–Schwarz inequality. Hence, in view of Eq. (F2), we find that

$$\mathbb{E}_{s \in C_l} \mathcal{D}[\rho_s, \tau_s] = O(N^{-c/4}). \quad (\text{F5})$$

Coming back to our setup, let  $\rho_X(t)$  be the state of the lattice  $X$  at the moment of time  $t$ , and  $T_X^{\text{eff,can}}(t)$  be its effective canonical temperature, as per the definition (8). Also let

$$\tau_X^{\text{eff,can}}(t) := \tau(T_X^{\text{eff,can}}(t), H_X) \quad (\text{F6})$$

be the Gibbs state corresponding to it. Now, observing that, due to Eq. (8),

$$S(\rho_X(t) \| \tau_X^{\text{eff,can}}(t)) = S(\tau_X^{\text{eff,can}}(t)) - S(\rho_X(t)),$$

where  $S(\rho)$  is the von Neumann entropy, and keeping in mind Eqs. (F5) and (2), we can state the following consequence of Proposition 2 of Ref. [50] and Lemma 2 of Ref. [55].

**Corollary F.1 (of Proposition 2 of Ref. [50])** *If  $\tau_X^{\text{eff,can}}(t)$  has exponentially decaying correlations and*

$$S(\tau_X^{\text{eff,can}}(t)) - S(\rho_X(t)) = o(N^{\frac{1-c(d+2)}{d+1}}), \quad (\text{F7})$$

*then  $\rho_X(t)$  is  $g$ -locally thermal at (almost) uniform temperature  $T_X^{\text{eff,can}}(t)$ , up to a correction  $\propto N^{-c/4}$ . The  $g$ -local thermality of  $X$  is at the level of subsystems of diameter  $l = o(n^{\frac{1-c}{d+1}})$  [Eq. (F3)].*

This result provides a background against which we can assess how “expected” the all-time  $g$ -local thermality result in Sec. IV is for short-range Hamiltonians. Indeed,

when  $H_X$  is finite-ranged and gapped,  $\tau(T, H_X)$  has exponentially decaying correlations at any  $T$  [119]. So, the first condition of Corollary F.1 is satisfied.

The validity of the second condition is in general much harder to assess a priori. But given that the entropy difference in Eq. (F7) is zero at  $t = 0$  in our setting, it would not be too surprising if it were to remain small enough to never violate Eq. (F7) during the evolution. This is so especially when  $H_{\text{int}}$  is invariant under translations in  $X$  (e.g., FB coupling), since in that case, one expects that both  $\tau_X^{\text{eff,can}}(t)$  and  $\rho_X(t)$  will remain translationally invariant (except for the edges) at all times.

We emphasize that Corollary F.1 has no bearing on the degree of validity of the condition (F7). Thus, it does *not* prove all-time  $g$ -local thermality of  $X$  when  $H_X$  is short-ranged and gapped and  $H_{\text{int}}$  is translationally invariant. However, the Corollary does show that it is not unexpected that we do observe all-time  $g$ -local thermality for such systems. In fact, when  $A$  and  $B$  are FB-coupled 2D lattices with nearest-neighbor interactions, we see in the bottom inset of Fig. 8 that  $g$ -local thermality is accompanied by  $T_X^{\text{eff}}(t) \approx T_X^{\text{eff,can}}$  at all times. This suggests (but does not prove) that Corollary F.1 applies in this case.

The situation changes, even for short-ranged  $H_X$ ’s, when  $H_{\text{int}}$  is not translationally invariant; e.g., in the case of EE coupling. Then, due to the gradients of energy (and temperature), the condition (F7) becomes unlikely to be satisfied at all times. By directly looking at  $\mathbb{E}_{s \in C_l} \mathcal{D}[\rho_s, \tau_s]$ , we indeed see that Eq. (F5) is violated. Let us consider, for concreteness, the [1D, EE] case for which Fig. 12 is plotted. Each single-site subsystem is almost exactly  $g$ -locally thermal, so, noticing that  $C_1$  is simply the set of all sites of  $X$ , we can write

$$\mathbb{E}_{s \in C_1} \mathcal{D}[\rho_s, \tau_s] = \frac{1}{N} \sum_{\nu=1}^N \mathcal{D}[\tau_{\nu}^{\text{MF}}(T_{\nu}^{\text{eff}}), \tau_{\nu}^{\text{MF}}(T_X^{\text{eff,can}})].$$

And since almost half of the sites of  $A$  are at  $T_{\nu}^{\text{eff}} \approx 0.5$  and the other  $\approx 25\%$  are at  $T_{\nu}^{\text{eff}} \approx 0.1$ , there exists some  $\zeta > 0$  such that  $\sum_{\nu=1}^N \mathcal{D}[\tau_{\nu}^{\text{MF}}(T_{\nu}^{\text{eff}}), \tau_{\nu}^{\text{MF}}(T_X^{\text{eff,can}})] \geq N\zeta$ . Hence,  $\mathbb{E}_{s \in C_1} \mathcal{D}[\rho_s, \tau_s] \geq \zeta$ , and therefore Eq. (F5) cannot hold for  $N \gg 1$ . Thus, Corollary F.1 does not apply. Nonetheless, both  $A$  and  $B$  remain  $g$ -locally thermal at all times, with very high accuracy, as Figs. 11 and 12 clearly illustrate.

Even further from the scope of Ref. [50], and consequently of Corollary F.1, are lattices with long-range interactions. In such systems, ensemble equivalence is known to generally fail [120, 121]. It is however worth noting that, in Ref. [52], it is proven that, for long-range interacting systems, microcanonical and canonical ensembles become equivalent at high temperatures. However, i) that result is only for microcanonical and canonical states, not for general states like Proposition 2 of Ref. [50], so it cannot be used in our scenario. And ii) for the values of interaction range  $\alpha \leq d$ , the threshold temperature above which the ensemble equivalence

is established in Ref. [52] diverges with  $N$ . In contrast, our all-time g-local thermality result holds for long-range interacting systems with arbitrary  $\alpha$  (Figs. 4 and 6 illustrate that for  $\alpha = 0.5$ ).

That the ensemble equivalence fails, whereas all-time g-local thermality persists, in the above two situations is a clear indication that the two phenomena are fundamentally different and independent from one another.

Lastly, we note that the results of Ref. [50], and therefore Corollary F.1, are proven only for lattices of systems with finite Hilbert-space dimension. In our case, however, the on-site Hilbert-space dimension is infinite. This is not a problem at finite temperatures—the on-site oscillators can be approximated by finite systems by simply cutting off the nearly unpopulated high-energy states. However, the higher the temperatures, the higher the cut-off dimension has to be. And while the increase of the on-site Hilbert-space dimension significantly weakens the bounds established in Ref. [50], interestingly, going to higher temperatures does not affect the precision of all-time g-local thermality in all the systems we tested.

### APPENDIX G: RATE EQUATION IN TTM

According to the TTM [21–27, 76], the energy exchange between two co-evolving systems is given by the equation

$$\begin{aligned}\frac{dE_A}{dt} &= -(T_A - T_B)k(T_A, T_B), \\ \frac{dE_B}{dt} &= -(T_B - T_A)k(T_A, T_B),\end{aligned}\tag{G1}$$

where the thermal conductance  $k(T_A, T_B)$  is positive provided heat flows from hot to cold.

Introducing the heat capacities for  $A$  and  $B$ , respectively, as  $C_A(T_A)$  and  $C_B(T_B)$ , we find the time evolution equation for the temperatures (recalling that the TTM assumes that  $A$  and  $B$  are thermal at all times)

$$\begin{aligned}\frac{dT_A}{dt} &= -(T_A - T_B)\frac{k(T_A, T_B)}{C_A(T_A)}, \\ \frac{dT_B}{dt} &= -(T_B - T_A)\frac{k(T_A, T_B)}{C_B(T_B)}.\end{aligned}\tag{G2}$$

Keeping in mind that  $C_A$  and  $C_B$  are positive quantities, we introduce

$$J(T_A, T_B) := k(T_A, T_B)\left[\frac{1}{C_A(T_A)} + \frac{1}{C_B(T_B)}\right] \geq 0,\tag{G3}$$

and obtain

$$\frac{d(T_A - T_B)}{dt} = -(T_A - T_B)J(T_A, T_B),\tag{G4}$$

This leads us to

$$T_A(t) - T_B(t) = [T_A(0) - T_B(0)]e^{-\int_0^t ds J(T_A(s), T_B(s))},\tag{G5}$$

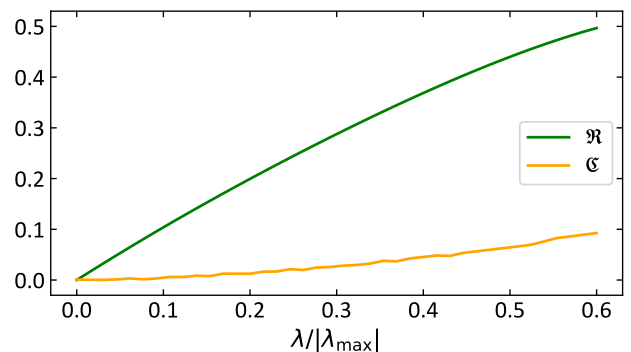


FIG. 16: **(Role of interaction energy at equilibrium.)** The plot shows that while, at long times,  $H_{\text{int}}$  stores a significant amount of energy (green line), its effect on the validity of Eq. (16) remains largely negligible even at strong couplings (orange line). Here  $\mathfrak{R}$  [Eq. (H1)] measures the share of  $H_{\text{int}}$  in the energy balance at equilibrium and  $\mathfrak{C}$  [Eq. (H2)] quantifies the precision to which Eq. (16) is satisfied (with general  $T_A^{\text{eq}}$  and  $T_B^{\text{eq}}$ ). We see that  $\mathfrak{C} \ll 1$  holds as long as the system equilibrates, and the choice of  $\lambda \leq 0.6|\lambda_{\text{max}}|$  here ensures that it does. All other parameters are the same as in Fig. (10).

which indeed proves that  $|T_A(t) - T_B(t)|$  monotonically decreases as the term in the exponent monotonically grows due to  $J$  remaining positive at all times.

In fact, the reverse statement is also true: any two monotonically converging, differentiable functions  $T_A(t)$  and  $T_B(t)$  are a solution to a rate equation of the form (G2). To see this, we notice that one can “reverse engineer” Eq. (G5) to obtain the function  $J(T_A(t), T_B(t))$ , by taking the derivative of  $T_A(t) - T_B(t)$ . Next, since the heat capacities  $C_A(T_A)$  and  $C_B(T_B)$  are given, Eq. (G3) can be solved for  $k(T_A(t), T_B(t))$ . By construction, the solution of the equation (G2) with the thus-obtained  $k(T_A, T_B)$  will yield the given functions  $T_A(t)$  and  $T_B(t)$ . Admittedly, this procedure is not useful in practical situations, it is presented here merely to prove the existence of a rate equation.

To summarize, the rate equation (G1) and the monotonicity of the convergence of  $T_A$  and  $T_B$  are equivalent statements. Thus, the second postulate of the TTM can be equivalently rephrased as: “the temperatures of the two systems approach each other monotonically in time.”

### APPENDIX H: ENERGY OF INTERACTION AT EQUILIBRIUM

Here we compare the share of  $H_{\text{int}}$  in the total energy at equilibrium with the precision to which Eq. (16) is satisfied.

The former is given by

$$\mathfrak{R} := \frac{\langle H_{\text{int}} \rangle^{\text{eq}}}{\langle H_A \rangle^{\text{eq}} + \langle H_B \rangle^{\text{eq}}},\tag{H1}$$

where  $\langle H_{\text{int}} \rangle^{\text{eq}} = \text{Tr}[H_{\text{int}} \rho_{AB}^{\text{GGE}}]$ , with the other two averages defined analogously. The “precision” of Eq. (16) is quantified by

$$\mathfrak{C} := 1 - \frac{\langle H_A \rangle_{T_A^{\text{eff,eq}}} + \langle H_B \rangle_{T_A^{\text{eff,eq}}}}{\langle H_A \rangle_{T_A} + \langle H_B \rangle_{T_B}}, \quad (\text{H2})$$

with all the averages defined as in Eq. (16).

We numerically observe that  $\mathfrak{C} \ll 1$  even for large values of  $\lambda$ , provided  $AB$  equilibrates at long times. This

is contrasted by the fact that  $\langle H_{\text{int}} \rangle^{\text{eq}}$  can be significant as compared to  $\langle H_A \rangle^{\text{eq}} + \langle H_B \rangle^{\text{eq}}$ . These aspects are illustrated in Fig. (16), where we see that  $\mathfrak{C} \leq 0.1$  (in fact remaining much lower than 0.1 up until  $\lambda/\lambda_{\text{max}} \approx 0.3$ ), whereas  $\mathfrak{R}$  grows almost linearly with  $\lambda$ , becoming as large as  $\approx 0.5$ .

Lastly, note that, when  $T_A^{\text{eff,eq}} \neq T_B^{\text{eff,eq}}$ , Eq. (16) will not be enough to determine both of these equilibrium temperatures.